An observational determination of the evolution of planetary nebulae

Guido van der Wolk*

March 1, 2006

Report of 'Groot onderzoek' done under the supervision of Prof. Dr. S.R. Pottasch at the Kapteyn Astronomical Institute of the University of Groningen

Abstract

For a sample of 23 Galactic planetary nebulae, selected on the basis of distance certainty and temperature of the central stars being below $T < 70,000$ K, central star Zanstra luminosities are determined. This has been done by obtaining magnitudes, interstellar extinctions and Zanstra temperatures. The magnitudes are determined from CCD images taken through a narrow band $H\alpha r$-filter centered at a wavelength $\lambda 6648 \mathring{A}$ and transposing the fluxes found towards the visual. The extinctions are found by at the same time obtaining images taken through a $H\alpha$-filter centered at $\lambda 6566 \mathring{A}$. The ratio of the resulting nebular line $H\alpha$-fluxes and $6cm$ or $21cm$ radio flux densities gives the extinction. The extinctions can be deduced from catalogued $H\alpha/H\beta$-ratios and the Galactic dust map of Schlegel et al. (1998) as well. The Zanstra temperatures are obtained from the ratio of the ionizing and the visual photons emitted by the star, $F(H\alpha)(6566)/F_{vis}(5450)$. For this method to work it is assumed that the central star radiates as a blackbody and the optical depth of the hydrogen ionizing radiation is greater than unity.

The positions of the central stars along with their ages are plotted in a Hertzsprung-Russell-diagram for each of the four methods used to determine the extinction. The ages are determined by dividing the radii of the planetary nebulae with their expansion velocities. Then this observational determination of the evolution of planetary nebulae is compared to the theoretical evolution-tracks of Blöcker (1995) calculated for stars with core masses ranging from $0.53 - 0.94$ M$_{\odot}$. All the four plots indicate that there are a low number of planetary nebulae in the sample with high stellar mass and a large number of planetary nebulae with low masses. The observationally found ages of the high mass objects are larger, while the low mass objects have smaller ages than theory predicts. This observational determination shows that the theory of the evolution of planetary nebulae must be revised.

*E-mail: wolk@astro.rug.nl

1 Introduction

Evolution of the central stars of planetary nebulae (PNe) is generally discussed in terms of an Hertzsprung-Russell diagram. This is a plot of the temperature or color of the star versus its luminosity. Currently existing evolutionary models have revealed unambiguously that the short-lived stage of planetary nebula evolution takes place in between the asymptotic giant branch (AGB) and white dwarf stage (see figure 1). Theoretical calculations have also shown that only stars with low to intermediate initial masses between 1 and 7 $M_{\odot}$ will develop a nebula at this stage of evolution and that the rate of evolution through the PN phase and the luminosity are heavily dependent upon the mass of the central star, which ranges from 0.53 to 0.94 $M_{\odot}$. Unfortunately, determinations of the temperature, luminosity and age of several nearby nebulae indicate a discrepancy between theory and observation: for luminous objects observational ages are larger, and for lower-luminosity objects observational ages are smaller than theory predicts (Mendez et al., 1988 and Gathier and Pottasch, 1989).

This result has not yet been taken seriously by workers in the field. Mainly because there are two basic problems in determining the luminosity. Firstly the distance is very uncertain for the nearby PNe, sometimes by more than 50 percent, and secondly luminosities determined from nebular line flux assume that all the central star ultraviolet radiation is absorbed by the nebula, which is an uncertain assumption.

To get around the distance problem one should limit oneself to studying planetary nebulae which are part of the Galactic bulge population. In this way PNe with distances at between roughly 7 and $9kpc$, which is an acceptable uncertainty of 15 percent, are selected. The second problem can be solved by determining the luminosity from a measurement of the central star instead of the nebular line flux. This involves a measurement of the magnitude and the extinction, which can often be considerable in the Galactic bulge. The magnitude measurement is extremely difficult because the nebular line flux must be excluded entirely from the observation. To do this fluxes with a narrow band redshifted $H\alpha r$ filter centered at a wavelength of $\lambda 6648\mathring{A}$, which has essentially no transmission at $H\alpha$ or the $[NII]$ lines, should be obtained. The only nebular line which is transmitted is the relatively weak HeI $\lambda 6678\mathring{A}$ line for which a correction can be made. By at the same time measuring the PN flux with a normal $H\alpha$-filter centered at a wavelength $\lambda 6566\mathring{A}$ the extinction can be calculated in conjunction with previously obtained radio, $6cm$ and $21cm$, continuum fluxes. Furthermore the extinctions can also be derived from observed Balmer line $H\alpha/H\beta$-ratios and the dust map of Schlegel et al. (1998).

This method will work as long as the stars are not extremely faint relative to

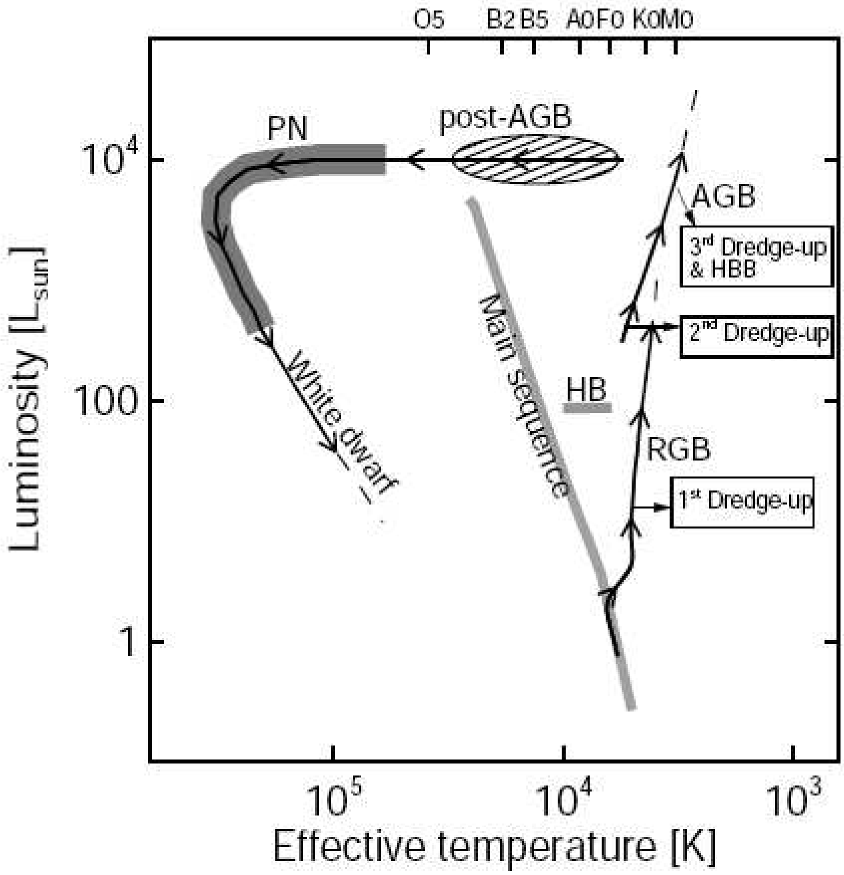

Figure 1: Hertzsprung-Russell diagram showing the evolution of a low mass star starting at the main sequence (MS) going up the red giant branch (RGB) and the asymptotic giant branch into the post-AGB phase and then the short-lived planetary nebula (PN) phase and finally the white dwarf stage. (J. Bernard-Salas, 2003).

the nebula, which will only occur in the case of very high temperature stars. So for a sample of Galactic bulge nebulae with known distances and central stars with a temperature below $T < 70,000$ K, which can be determined either from a energy balance method or the ratio of the nebular line fluxes $F([OIII](5007))$ and $F(H\beta)$ which should be less than about $[OIII]/H\beta < 8$, a sound luminosity determination can be made. This 'Groot onderzoek' deals with the reduction of such measurements, which have been obtained with the 91cm Dutch telescope of the European Southern Observatory (ESO) located at La Silla in Chile.

The HR-diagram resulting from these measurements will then be compared with the theoretical evolutionary tracks of Blöcker (1995), in which the billion years of evolution of 1, 3, 4, 5 and 7 M$_\odot$ stars from the zero age main sequence (ZAMS) through the AGB towards the stage of white dwarfs are calculated. The cores of these stars, which form a major part of our galaxy, are believed not to go beyond the helium burning phase. The temperature in the core will not become high enough for carbon to fuse. If all the helium in the core is burnt into carbon the center becomes more dense while the outer layers will expand as a reaction. Now the star is on the AGB in the Hertzsprung-Russell diagram. When the fusion in the core ceases, the star consists of a carbon core with around it a helium and hydrogen burning shell. It is assumed that it then becomes unstable to a large mass loss and throws off up to fifty percent of its mass. This material consists mainly of hydrogen while a carbon core with a helium envelope is left as the central star. When the star becomes hot enough it ionizes the surrounding nebula

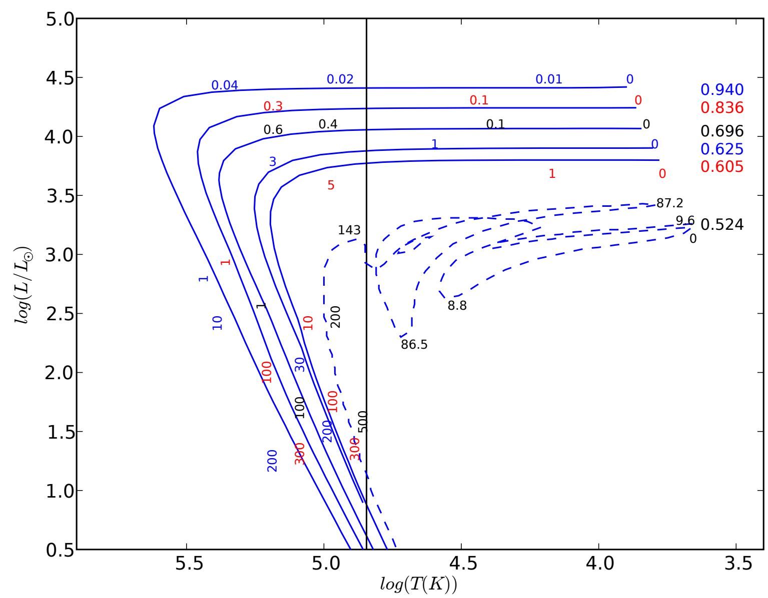

Figure 2: The theoretical evolutionary tracks of planetary nebulae calculated by Blöcker (1995) for central stars with $(M_{ZAMS}, M_H) = (1\ \mathrm{M}_\odot, 0.524\ \mathrm{M}_\odot)$, undergoing two thermal pulses, $(3\ \mathrm{M}_\odot, 0.605\ \mathrm{M}_\odot)$, $(3\ \mathrm{M}_\odot, 0.625\ \mathrm{M}_\odot)$, $(4\ \mathrm{M}_\odot, 0.696\ \mathrm{M}_\odot)$, $(5\ \mathrm{M}_\odot, 0.836\ \mathrm{M}_\odot)$ and $(7\ \mathrm{M}_\odot, 0.940\ \mathrm{M}_\odot)$. The ages are indicated in units of 10^3 yr. The central stars of PNe with temperatures below $70,000$ K are on the horizontal track. A star with 0.940 M$_\odot$ will spend a meagre 20 yr, a 0.605 M$_\odot$ star a larger 4000 yr and a 0.524 M$_\odot$ helium burner up to $14,000$ yr of evolution on the horizontal track. (Reproduced from the calculations of Blöcker (1995).

and a planetary nebula arises, living its life on the horizontal track, see figure 2. The nebula gets larger and the temperature of the central star increases, while the luminosity remains the same, forcing the radius to decrease. Then the PN moves down the HR-diagram, until it becomes too faint to be observed any longer. It has then entered the white dwarf stage.

The calculations of Blöcker (1995) are based on stars for which the initial chemical composition is taken as $(X, Y, Z) = (0.739, 0.24, 0.01)$ and the relation between the ZAMS and core masses is consistent with empirical initial-final masses which have been determined by Weidemann (1987). According to these models a PN with a temperature below $T < 70,000$ K and a core mass of 0.940 $M_\odot$ spends a meagre 20 yr, a 0.605 $M_\odot$ star a larger 4000 yr and a 0.524 $M_\odot$ helium burner up to $140,000$ yr of evolution on the horizontal track. In the last model, with $(M_{ZAMS}, M_H) = (1\ M_\odot, 0.524\ M_\odot)$, two evolution loops occur. At $t = 8400$ yr the helium shell gets thermally unstable leading to a luminosity drop which is followed by a evolution back to the vicinity of the AGB. The post-AGB evolution starts again and 3000 yr later the hydrogen reignites leading to an increase of the luminosity. A second thermal pulse takes place at $t = 86,000$ yr. Because this instability is much more stronger than the first one the corresponding loop in the HR-diagram is more pronounced. These calculations indicate that more massive stars evolve faster on the horizontal track than low mass stars. However, if one looks at the total lifetimes massive stars fade much more slowly. For instance at $\log L/L_\odot = 2.1$ the PN age of the 0.836 $M_\odot$ model amounts to $60,000$ yr, being twice as large as the corresponding age of the 0.605 $M_\odot$ remnant.

The goal of this 'Groot onderzoek' is to determine the interstellar extinction, temperature, luminosity and ages of Galactic bulge planetary nebulae that lie on the horizontal track of the evolution stage and compare this with theoretical calculations. If agreement is found the theory may be correct. If there is disagreement the theory must be revised. In chapter 2 the observational methods used, i.e. collecting the data and the data reduction, are discussed. Chapter 3 deals with the theory of determining the interstellar extinction, temperature, visual magnitudes, luminosities and ages. In chapter 4 the results are presented, which are discussed in chapter 5. In chapter 6 the conclusions are summarized.

2 Observations and reductions

The observations of the planetary nebulae (PNe) were made with the Dutch 91cm telescope of the European Southern Observatory (ESO), located at La Silla in Chile, by Paul Groot (July, 1993), Remco Schoenmakers (June/July, 1994) and Martin Zwaan and Paul Vreeswijk (June/July, 1995). CCD images were obtained of the PNe in narrow band filters $H\alpha$, $H\alpha r$, $H\beta$ and $OIII$. Furthermore images of standard stars were obtained in the filters $H\alpha$, $H\alpha r$, $H\beta$, Y, U, B, V, R and I. Each observing night also bias frames and flat-field exposures were made. The data tapes and observation logs were obtained from the archives of the Kapteyn Instituut, Sterrewacht Leiden and Sterrenkundig Instituut Anton Pannekoek in Amsterdam. The observing run of Paul Groot was previously analysed by Paul Vreeswijk (1995) who used ESO's Munich Image Data Analysis System (MIDAS). Here the data obtained by Paul Groot and the two newer observing runs, providing 21 observation nights in total, are analyzed using NOAO's Image Reduction and Analysis Facility (IRAF). For the reduction the IRAF tutorials of Massey and Davis (1992) and Massey (1997) are used.

2.1 Sample selection

The sample consists of 27 Galactic planetary nebulae in total. Of these 23 are located in the Galactic bulge; 1 in the globular cluster M15, namely Ps1; PN G009.4-05.0 (see figure 6) is a nearby one, discovered by Herschel in 1868. BoBn1 and PHL932 are 2 other Galactic PNe with known distances. All of the PNe are observed with in narrow band filters $H\alpha$ and $H\alpha r$, some multiple times with different exposure times and some also in $H\beta$ and $OIII$. This is listed in table 1. The designation system of the planetary nebulae has the structure: PN Glll.l+bb.b where PN means *Planetary Nebula*, G stands for *Galactic Coordinates*, and lll.l+bb.b stand for the Galactic longitude and latitude respectively, truncated to one decimal place.

The selection of this sample is based on the distances of the PN and the temperatures of the central stars. Distances of the PNe that are part of the Galactic bulge population are known best with an uncertainty of 15 percent, being in the order of $8.0 \pm 1.2 kpc$. The temperatures of the central stars of the PNe are below $T < 70,000$ K. This can be determined from the previously observed ratios of nebular line fluxes $F([OIII](5007))$ and $F(H\beta)$ which should be less than about $[OIII]/H\beta < 8$. For higher temperatures the central star becomes too faint relative to the nebula for the method used to work.

name	PNG	date	R.A.2000	δ2000	$t(s)$	filters
H1-62	000.0-06.8	13/7 - 14/7/1993	18 13 18.03	-32 19 43.0	1200	$H\alpha$, $H\alpha r$
H1-62	000.0-06.8	24/6 - 25/6/1994	18 13 18.03	-32 19 43.0	300	$H\alpha$
H2-40	000.1-05.6	13/7 - 14/7/1993	18 08 24.92	-31 37 24.3	1200	$H\alpha$, $H\alpha r$
H2-40	000.1-05.6	25/6 - 26/6/1994	18 08 24.92	-31 37 24.3	900	$H\alpha$
H2-11	000.7+04.7	21/7 - 22/7/1993	17 29 25.97	-25 49 23.0	1200	$H\alpha$, $H\alpha r$
H2-11	000.7+04.7	24/6 - 25/6/1994	17 29 25.97	-25 49 23.0	1200	$H\alpha$
H1-47	001.2-03.0	11/6 - 12/6/1994	18 00 37.60	-29 21 50.2	600,1800	$H\alpha$, $H\beta$, $OIII$
H1-47	001.2-03.0	13/6 - 14/6/1994	18 00 37.60	-29 21 50.2	1500	$H\beta$
H1-15	001.4+05.3	20/7 - 21/7/1993	17 28 37.38	-24 51 05.5	1200	$H\alpha$, $H\alpha r$
H1-55	001.7-04.4	19/7 - 20/7/1993	18 07 14.58	-29 41 24.0	1200	$H\alpha$, $H\alpha r$
H1-55	001.7-04.4	13/6 - 14/6/1994	18 07 14.58	-29 41 24.0	900,1800	$H\alpha$, $H\beta$
H2-43	003.4-04.8	18/7 - 19/7/1993	18 12 47.98	-28 20 01.0	900	$H\alpha$, $H\alpha r$
H2-43	003.4-04.8	11/6 - 12/6/1994	18 12 47.98	-28 20 01.0	600	$H\alpha$
M2-37	004.2-05.9	24/7 - 25/7/1993	18 18 38.73	-28 08 05.4	1200	$H\alpha$, $H\alpha r$
M2-37	004.2-05.9	16/6 - 17/6/1994	18 18 38.73	-28 08 05.4	900	$H\alpha$
H1-24	004.6+06.0	24/7 - 25/7/1993	17 33 37.75	-21 46 17.6	1200	$H\alpha$, $H\alpha r$
H1-24	004.6+06.0	16/6 - 17/6/1994	17 33 37.75	-21 46 17.6	900	$H\alpha$
H1-58	005.1-03.0	24/7 - 25/7/1993	18 09 13.42	-26 02 26.5	1200	$H\alpha$, $H\alpha r$
Hf2-2	005.1-08.9	11/7 - 12/7/1993	18 32 31.10	-28 43 21.1	1200	$H\alpha$, $H\alpha r$
Hf2-2	005.1-08.9	25/6 - 26/6/1993	18 32 31.10	-28 43 21.1	900	$H\alpha$
Hf2-2	005.1-08.9	11/6 - 12/6/1993	18 32 31.10	-28 43 21.1	900	$H\alpha$
H1-64	008.4-03.6	12/7 - 13/7/1993	18 32 34.77	-25 07 43.9	1200	$H\alpha$, $H\alpha r$
NGC6629	009.4-05.0	11/7 - 12/7/1993	18 25 43.48	-23 11 59.3	1200	$H\alpha$, $H\alpha r$
NGC6629	009.4-05.0	24/6 - 25/6/1994	18 25 43.48	-23 11 59.3	600	$H\alpha$
NGC6629	009.4-05.0	25/6 - 26/6/1994	18 25 43.48	-23 11 59.3	120	$H\alpha$
NGC6629	009.4-05.0	11/6 - 12/6/1994	18 25 43.48	-23 11 59.3	120	$H\alpha$
NGC6629	009.4-05.0	13/6 - 14/6/1994	18 25 43.48	-23 11 59.3	120,300	$H\alpha$, $H\beta$
NGC6629	009.4-05.0	16/6 - 17/6/1994	18 25 43.48	-23 11 59.3	120	$H\alpha$
Ps1	065.0-27.3	07/7 - 08/7/1995	21 29 59.4	+12 10 26	900	$H\alpha$, $H\alpha r$
Ps1	065.0-27.3	09/7 - 10/7/1995	21 29 59.4	+12 10 26	1200	$H\beta$
BoBn1	108.4-76.1	05/7 - 06/7/1995	00 37 16.03	-13 42 58.5	600	$H\alpha$, $H\alpha r$
BoBn1	108.4-76.1	05/7 - 06/7/1995	00 37 16.03	-13 42 58.5	900	$H\beta$
PHL932	125.9-47.0	01/7 - 02/7/1995	00 59 56.67	+15 44 13.7	800	$H\alpha$, $H\alpha r$, $H\beta$
M2-5	351.2+05.2	13/7 - 14/7/1993	17 02 19.14	-33 10 03.9	1200	$H\alpha$, $H\alpha r$
M2-10	354.2+04.3	18/7 - 19/7/1993	17 14 07.04	-31 19 42.3	1200	$H\alpha$, $H\alpha r$
Th3-6	354.9+03.5	19/7 - 20/7/1993	17 19 20.54	-31 12 33.8	1200	$H\alpha$, $H\alpha r$
M1-30	355.9-04.2	10/7 - 11/7/1993	17 52 59.01	-34 38 23.0	1200	$H\alpha$, $H\alpha r$
H1-39	356.5-03.9	25/6 - 26/6/1993	17 53 21.00	-33 55 58.4	900	$H\alpha$, $H\alpha r$, $H\beta$
Th3-12	356.8+03.3	20/7 - 21/7/1993	17 25 06.46	-29 45 14.9	1200	$H\alpha$, $H\alpha r$
Al2-H	357.2+01.4	23/7 - 24/7/1993	17 33 17.03	-30 26 30.6	1200	$H\alpha$, $H\alpha r$
TH3-23	358.0+02.6	21/7 - 22/7/1993	17 30 23.69	-29 09 34.0	1200	$H\alpha$, $H\alpha r$
M3-40	358.7+05.2	19/7 - 20/7/1993	17 22 28.31	-27 08 35.2	1200	$H\alpha$, $H\alpha r$
Th3-15	358.8+04.0	20/7 - 21/7/1993	17 27 09.50	-27 44 24.0	1200	$H\alpha$, $H\alpha r$
Al2-G	359.0+02.8	23/7 - 24/7/1993	17 32 22.56	-28 14 30.4	1200	$H\alpha$, $H\alpha r$

Table 1: Sample of observed PNe grouped by name, designation, observing night, right ascension and declination for the epoch 2000, exposure time t and the filters used.

2.2 Instrumental parameters

The Dutch 91cm telescope has been installed at La Silla in 1970 after being at Hartebeespoortdam in South Africa for many years, and equipped with a Walraven photometer. It is a reflecting telescope built by Rademakers of Rotterdam in the 1950's. Since 1991 the telescope is equipped with a CCD direct imaging Cassegrain adapter with two filter wheels, holding seven filters each, and an autoguider. The mirrors are Dall-Kirkham type, i.e. an elliptical primary and a spherical secondary mirror. The primary mirror has a diameter of 91 centimeter and is a $f/3.52$ telescope. The whole telescope is a $f/13.75$. The Cassegrain plate scale is 16.52 arcseconds per millimeter.

In the observing runs of Paul Groot, Martin Zwaan and Paul Vreeswijk the adapter is equipped with ESO chip number 33 and in the run of Remco Schoenmakers with ESO chip number 29. These are TEK CCD's with 512×512 pixels each of size 27 micrometer on the side. This results in images consisting of 580 columns and 520 rows of pixels, with a prescan extending over the first 50 columns and overscans extending over the last 18 columns and the last 8 rows. A pixel projects $0.442''$ on the sky, providing a field of view of $3'77''$ square.

Furthermore the efficiency, bandwidth and sensitivity for atmospheric extinction at La Silla of each filter are important instrumental parameters. This information can be found on the ESO website. The values are listed in table 2. The atmospheric extinctions are wavelength-dependent and specific for La Silla. They have been obtained from extensive measurements done by Tug (1977), us-

Filter	Name	CWL ($\AA$)	FWHM ($\AA$)	Extinction e (magnitude/airmass)
387	$H\alpha$	6566	82.27	0.05±0.01
389	$H\alpha r$	6648	78.88	0.05±0.01
750	$H\beta$	4856	75.22	0.15±0.01
714	Y	5483	182.51	0.11±0.01
688	$OIII$	5007	56.19	0.13±0.01
634	U	3543	539.47	0.50±0.20
419	B	4333	1020.11	0.22±0.11
430	V	5442	1170.73	0.11±0.06
421	R	6481	1645.49	0.06±0.04
465	I	7972	1407.37	0.02±0.01

Table 2: The ESO filter number and name with its central wavelength (CWL), full width at half maximum (FWHM) and the wavelength-dependent atmospheric extinction e in magnitude/airmass specific for La Silla as measured by Tug (1977).

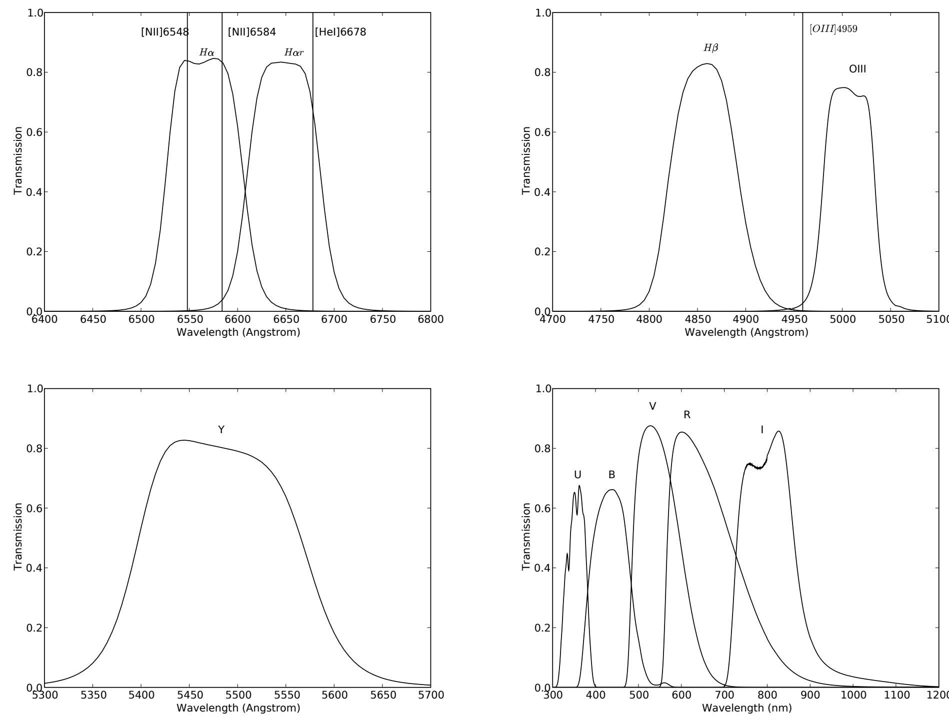

Figure 3: Transmission curves for the $H\alpha$, $H\alpha r$, $H\beta$ and $[OIII]$-filters used to determine the fluxes of the PNe and Hamuy et al. (1992) standard stars at these wavelengths and U,B,V,R and I filters used to determine the fluxes of Landolt (1992) standard stars.

ing the 0.6-m Bochum telescope at La Silla. The errors were estimated from the bandwidths of the filters. Transmission curves of the filters are shown in figure 3. The $H\alpha$-filter, with ESO number 387, is centered around a wavelength of $\lambda 6566\mathring{A}$ having a full width at half maximum (FWHM) of $82.27\mathring{A}$ and the $H\alpha r$-filter, with number 389, at $6648\mathring{A}$ having a FWHM of $78.88\mathring{A}$. In images of PNe made with both these filters emission lines will be present: two forbidden [NII] lines at $6548\mathring{A}$ and $6584\mathring{A}$ in the Hα-images and a relatively weak HeI line at $6687\mathring{A}$ in the Hαr-images. For the $OIII$-filter, centered at the emission line [OIII](5007), a tiny fraction of emission of the $[OIII]$(4959)-line will be present in the PN-images. For the $H\beta$ no other emission lines will be present. The Y, U, B, V, R and I-filters used for determining the fluxes of the standard stars have larger integrated widths.

However, due to temperature differences, uncollimated beams or ageing of the filters the actual transmitted wavelengths could be bluer than the transmission curves of figure 2. This shift can be as large as $20\mathring{A}$. So one should be cautious about the lines on the edges of the transmission curves. For the $H\alpha$-filter such a shift hardly excludes any $[NII](6584)$ emission and the HeI(6678) emission line in the $H\alpha r$-filter will not decrease significantly either. But such a shift would increase emission of the $[OIII](4959)$-line in the $OIII$-filter. These shifts would also influence the measured fluxes of the standard stars, which are used to calibrate the PN-fluxes.

2.3 Data preparation

To prepare the data, directories with all the relevant image files of the *bias frames*, *flatfield exposures*, the standard stars and the PNe have to be made for each of the 21 observing nights. *Bias frames* are zero length exposures and *flatfield exposures* are uniform exposures of all pixels used to map out the sensitivity of each pixel. Standard stars, for which the fluxes are known, are used to calibrate the number of counts of an object into a flux.

To prepare the data further, IRAF is started in a xgterm with a scrollbar, `xgterm -sb`, with the command `cl`. The files can be examined and displayed with the commands `imexamine` and `display`. Firstly, the gain and readnoise of the CCD are determined with `findgain`, available in the OBSUTIL package which asks for two bias frames and two flat field exposures as input. The task requires that the flats and zeros sequence each other. Furthermore they have to be unprocessed and uncoadded so that the noise characteristics of the data are preserved. For the method to work an area in the flats and zeros should be chosen where there are no bad pixels present. The gain G is calculated via Janesick's method in electrons per ADU, the Analog to Digital Unit or count, using

$$G = \frac{(\mu_{f1} + \mu_{f2}) - (\mu_{z1} + \mu_{z2})}{\sigma^2_{f1-f2} - \sigma^2_{z1-z2}} \frac{electrons}{ADU}, \tag{1}$$

where μ_{f1} and μ_{f2} are the means of the flats, μ_{z1} and μ_{z2} are the means of the zeros and σ_{f1-f2} and σ_{z1-z2} the variance of the difference between the flats and the zeros respectively. The readnoise RN, in electrons, is determined by

$$RN = G\frac{\sigma_{z1-z2}}{\sqrt{2}} electrons. \tag{2}$$

Secondly, the header files have to be edited. The names of the zero frames should be put in a file with `files name1 name2 > biasfiles` and then with a `ccdhedit @biasfiles imagetype zero` the command, available in the CCDRED package, headers are extended with the information that the file is a bias frame. This also has to be done with the flatfields, that should get the extension *flat* in their headers. The standard stars and the PNe should get the extension *object*. The files can be listed with `ccdlist` to check if the files have got their new extensions.

Thirdly, in order to determine the prescan, overscan and the area of the chip that contains good data a flatfield has to be examined using `implot` and some parameters can be set. IRAF needs to know with what type of instrument the data are made. This is set with `setinstrument direct` from within the CCDRED package. The pixeltype is set to `pixeltype=short real` to retain the 8-bit output images but arithmetic in floating point. Exiting `setinstrument` the parameters of `ccdproc` have to be filled in. The trimsection, the area of the chip with the good data, is set to `trimsec=[52:561,1:511]`. The biassection, the region of the overscan, is set to `biassec=[563:581,1:511]`. At this stage of the process only `overscan`, `trim` and `zerocor` are turned on and *Zero* is filled in as the name of the combined biasframe.

2.4 Bias subtraction

The output signal of the telescope is biased by adding a pedestal level of several hundred counts, ADU's. This bias level will vary with for instance telescope position, weather and temperature. Furthermore the bias level is usually a slight function of position on the chip, varying primarily along columns. This bias level is removed using the data in the *overscan* region, the 18 columns at the right edge of the frames. To remove the preflash of the chip, the light that falls in before an exposure of an object is even made, bias frames, with zero integration time, are obtained. This extra signal needs to be subtracted from the data. These bias frames, of which each observing night a new sequence of ten frames is made, are combined with `zerocombine @biasfiles output=Zero` in the CCDRED package and has as output an averaged zero frame called *Zero*. The averaging will ignore the highest values for each pixel. In other words, if there are ten bias frames, nine will be averaged in producing the value for each pixel in the image *Zero*, ignoring the highest value at each pixel. Now, to subtract the average bias and the overscan from the flatfields and the objects the task `ccdproc` is run. This task will also trim the images to fields of 512×512 pixels.

2.5 Dark current

On some CCD's there is a non-negligible amount of background added during long exposures. For this purpose dark exposures, long integrations with the shutter closed, are made. Inspecting these *darks* it shows that the current doesn't scale linearly. In the data set of Paul Groot only two dark frames are present. That is not enough. In order to remove radiation events at least three dark frames are required. Otherwise the signal-to-noise would decrease significantly. So the dark current, which for CCD chips TEK29 and TEK33 has typically a rate in the order of $6.5 \pm 1 electrons/pixel/hour$, is chosen not to be subtracted.

2.6 Flatfield division

In order to remove further detector signature the bias-subtracted and trimmed flat-field exposures should be combined for each filter separately and the resulting flats should be used to flatten the bias-subtracted objects. The data are divided by the flat-field in order to remove the pixel-to-pixel gain variations and some of the lower-order wavelength-dependent sensitivity variations. For instance, the Hα flats are combined with `flatcombine @FlatsHA output=FlatHA combine=average reject= crreject gain= gain readnoise=rdnoise` in the CCDRED package. This will combine the flats listed in the file *FlatsHa* with as output *FlatHa*. Radiation events are eliminated by *crreject*. The *gain* and *readnoise* from the CCD have to be known and have been determined with `findgain`. With the command `ccdproc @objectsHA flatcor+ flat=FlatHA` the objects listed in the file *objectsHA* are divided by the combined flatfield *FlatHA*. Checking the processed images the sky is mostly constant on a certain value but never zero.

2.7 Fixing cosmic rays

Cosmic rays are random events which can occur at any place on an image. In combining the flatfields these events are corrected for. But in order to clean the single images of the standard stars and the PNe, statistics should be used. The task `cosmicrays` in the CRUTIL package, searches for and corrects cosmic rays using selection criteria given by the parameters *threshold* and *fluxratio*. The *threshold* value determines the statistics used to identify deviant pixels and is set to five times the standard deviation in the background regions. The *fluxratio* parameter is used to choose which pixels should be corrected; they will be replaced with the mean of the four neighboring pixels. This parameter is the ratio of the flux, excluding the brightest neighbor, to that of the target pixel. A value of 5 implies that the target pixel's value must exceed the mean of its neighbors by a factor of 20 to be deleted. Setting the *fluxratio* to high can delete good data. Running this task interactively produces a plot of the pixels that could be cosmic rays, which are represented by crosses. Good points are represented by pluses. By increasing the fluxratio points which are clearly cosmic rays but are seen as good points can also be included. This procedure works pretty well but is not able to remove larger streaks cosmic rays leave on the image.

2.8 Standard star photometry and reductions

To obtain the flux in counts of the standard stars the basic steps are (1) deciding with what aperture size the standards are measured, which should be the same for all the frames, (2) setting up the various parameter files, `datapars`, `centerpars`, `fitskypars` and `photpars` in the DAOPHOT package, to get the correct values and (3) for each frame identifying the standard star with `daofind` and running the aperture photometry program `phot`.

An aperture size, the radius of the stellar image, is chosen of 18 pixels. This is the value of the FWHM times four to five. It isn't necessary to pick an aperture size that will contain all the light from the standard stars. In fact this is even impossible; the wings of a star's profile extend much further than imagined at a significant level. The parameter of the aperture size is set with the task `photpars`. The FWHM of a star image, the threshold value above sky and the gain and readnoise should be specified in `datapars`. In `centerpars`, which handles with determining the center of the star, the algorithm should be set to `centroid` and the size of the centering box set to `cbox=8`. In `fitskypars` the size and location of the annulus in which the modal value of the sky will be determined should be set to five pixels larger than the aperture, since the sky typically starts there. Then with `daofind` the stars in the image are found for which the procedure `phot` determines the counts for each of the stars and writes it to a file along with the exposure time and airmass, which values are taken from the header file.

If the airmass is not given in the header file of the image, it should be calculated and added using a small macro. To calculate the effective airmass the longitude and latitude of the Dutch telescope, the universal time and date, the exposure time and the right ascension and declination along with the epoch of the object has to be known. The procedure `asthedit` in the ASTUTIL package along with a programmed command list grabs these numbers from the header file and calculates the airmass at the middle of the exposure time and appends this information to the header.

The observed counts C have to be divided by the exposure time t, to get the number of counts per second, and corrected for the airmass m and the atmospheric extinction e in magnitudes/airmass (see table 2). Since 1 percent difference in magnitudes equals about 1 percent in flux, this can be done via

$$\phi = \frac{C}{t}(m \cdot e + 1)\frac{counts}{s}, \tag{3}$$

Then, these corrected fluxes have to be compared to the theoretical fluxes. These are acquired by multiplying the interpolated spectral energy distribution by the transmission curves of the filters and then integrating these functions (figures 4 and 5). The spectra are obtained from the southern hemisphere standard star catalogue of Hamuy et al. (1992) in steps of $50\AA$. For the Landolt (1992) standard stars no spectra are available, but just the V, B, R and I magnitudes (see table 3). These magnitudes have to be transformed from the Johnson-Morgan filter system to the Dutch telescope V, B, R and I-filters, which are centered on different wavelengths and have different integrated widths. The obtained theoretical fluxes $F(H\alpha)$, $F(H\alpha r)$, $F(H\beta)$, $F(B)$, $F(V)$, $F(Y)$, $F(R)$ and $F(I)$ of the Hamuy and

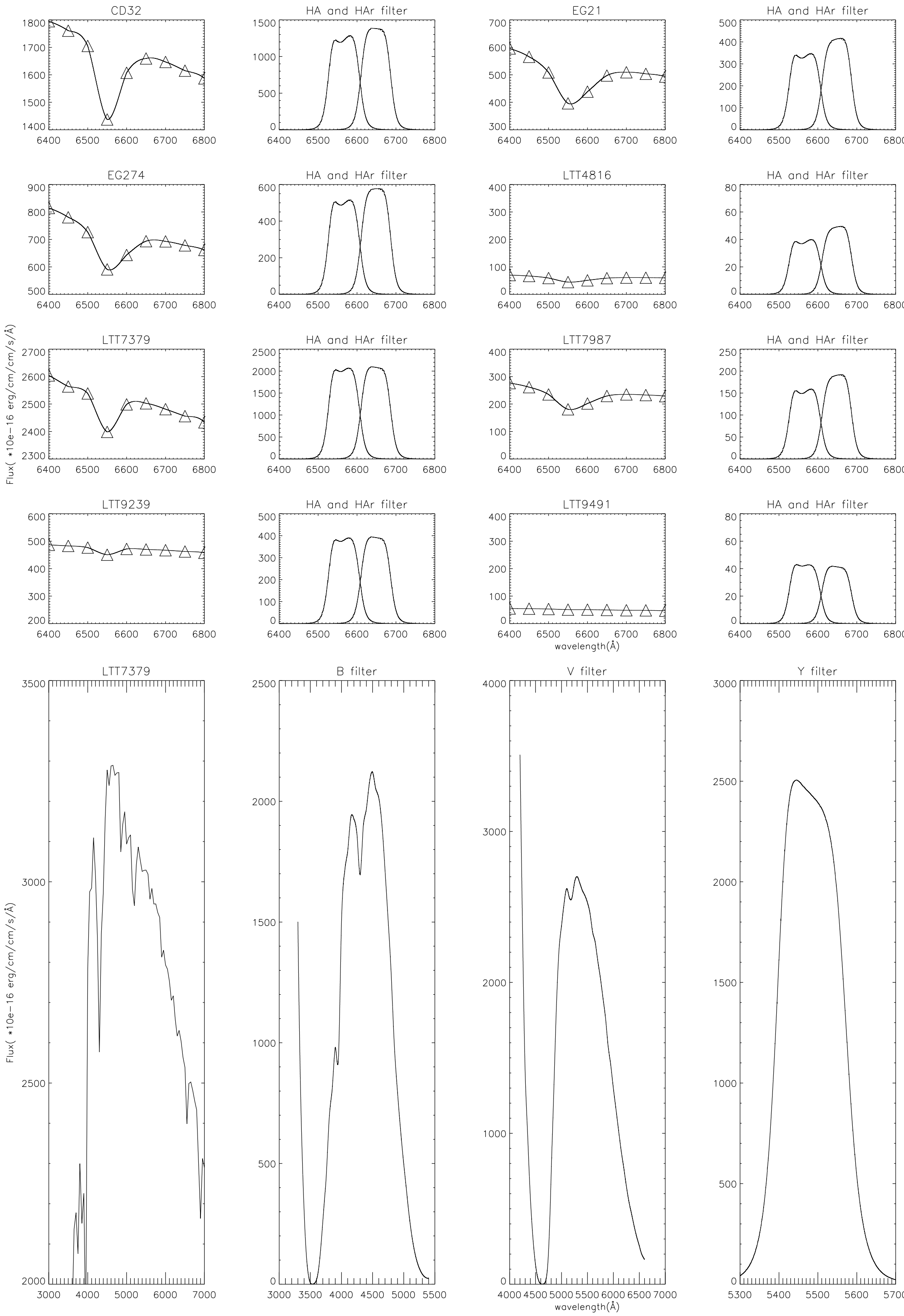

Figure 4: Spectra of Hamuy et al. (1992) standard stars CD32, EG21, EG274, LTT4816, LTT7379, LTT7987, LTT9239, LTT9491 (left) in steps of 50$\mathring{A}$ multiplied by the filter transmission curves for $H\alpha$ and $H\alpha r$ (right) and the spectrum of LTT7379 multiplied by the B, V and Y filter transmission.

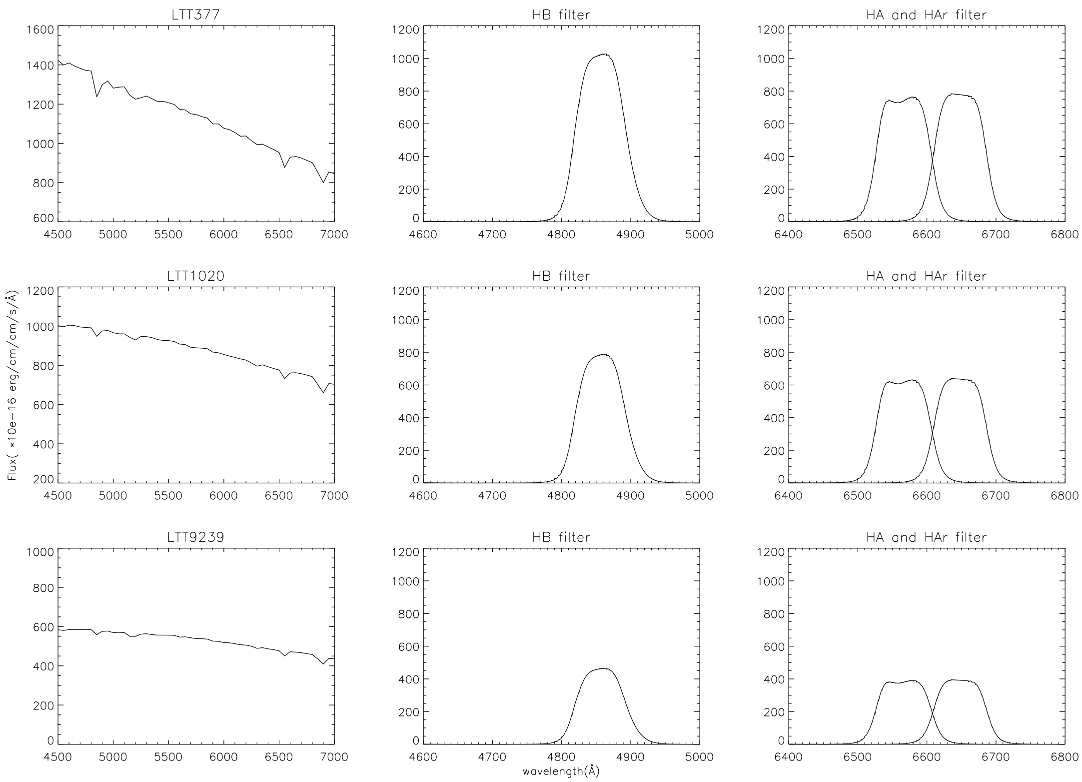

Figure 5: Spectra of Hamuy et al. (1992) standard stars LTT377, LTT1020 and LTT9239 (left) multiplied by the filter transmission curves for $H\beta$, $H\alpha$ and $H\alpha r$ (right).

Standard star	V	B	R	I
PG1323-086A	13.59	13.98	13.34	13.09
PG1323-086B	13.41	14.17	12.98	12.58
PG1323-086C	14.00	14.71	13.61	13.25

Table 3: Landolt (1992) star V, B, R, and I magnitudes obtained with the Johnson-Morgan filter system used to determine the fluxes in the V, B, R and I filters at the Dutch telescope.

Landolt standard stars in the different filters are listed in table 4. The errors are taken three percent for the Hamuy standard stars in the filters $H\alpha$, $H\alpha r$ and $H\beta$, ten percent for the filters B, V and Y and ten percent for the Landolt standard stars in the filters B, V, R and I. This takes into account the fact that these are spline-fitted values and a possible shift of the filters due to ageing or temperature differences.

To obtain the flux per count the theoretical flux is divided by the observed flux in counts per second of the standard stars for each night and each filter. These

Standard star	$F(H\alpha) \times 10^{-12}$ $ergcm^{-2}s^{-1}$	$F(H\alpha r) \times 10^{-12}$ $ergcm^{-2}s^{-1}$		
CD32	10.88±0.330	11.19±0.336		
EG21	2.999±0.090	3.310±0.099		
EG274	4.432±0.133	4.640±0.139		
LTT4816	0.344±0.010	0.393±0.012		
LTT7379	17.5±0.530	16.96±0.509		
LTT7987	1.375±0.041	1.525±0.046		
LTT9491	0.364±0.011	0.337±0.010		
	$F(H\alpha) \times 10^{-12}$ $ergcm^{-2}s^{-1}$	$F(H\alpha r) \times 10^{-12}$ $ergcm^{-2}s^{-1}$	$F(H\beta) \times 10^{-12}$ $ergcm^{-2}s^{-1}$	
LTT377	6.456±0.194	6.322±0.190	8.153±0.245	
LTT1020	5.341±0.160	5.169±0.155	6.174±0.309	
LTT9239	3.296±0.099	3.196±0.096	3.639±0.109	
	$F(B) \times 10^{-12}$ $ergcm^{-2}s^{-1}$	$F(V) \times 10^{-12}$ $ergcm^{-2}s^{-1}$	$F(Y) \times 10^{-12}$ $ergcm^{-2}s^{-1}$	
LTT 7379	204.4±20.44	339.7±33.97	46.76±4.676	
	$F(B) \times 10^{-12}$ $ergcm^{-2}s^{-1}$	$F(V) \times 10^{-12}$ $ergcm^{-2}s^{-1}$	$F(R) \times 10^{-12}$ $ergcm^{-2}s^{-1}$	$F(I) \times 10^{-12}$ $ergcm^{-2}s^{-1}$
PG1323-086A	24.3±2.43	15.1±1.51	14.5±1.45	8.43±0.84
PG1323-086B	14.3±1.43	17.8±1.78	20.2±2.02	13.5±1.35
PG1323-086B	9.94±0.99	9.01±0.90	11.3±1.13	7.28±0.73

Table 4: Theoretical fluxes of the standard stars in the $H\alpha$, $H\alpha r$, $H\beta$, Y, $OIII$, U, B, V, R and I filters. By comparing these with the observed counts of the standard stars in the different filters the counts of the PNe can be calibrated into fluxes.

calibration-fluxes $N_{H\alpha}$, $N_{H\alpha r}$ and $N_{H\beta}$, in units of $ergcm^{-2}count^{-1}$, are shown in table 5. For nights 11 to 15 the calibration-fluxes N are not filter-specific, since the PNe are not observed with the filters B, V, R, I and Y. The mean values are given along with the uncertainties, calculated according to the error analysis in the appendix, taking account for the errors in the atmospheric extinction, the three to ten percent errors of the theoretical fluxes and a three percent uncertainty of the counts.

For each night some 10 to 20 standard star images were obtained, providing a good calibration-flux. Because there is a clear atmospheric-extinction-calibration-flux-correlation, if the airmass increases the calibration-flux increases, it is evident that obtaining a lot of standard stars gives the best indication of the instrumental parameters. Also it is evident that obtaining standard star images in each filter is preferable. For the observing run of 1993, it is seen that in general for each night $N_{H\alpha}$ increases as $N_{H\alpha r}$ increases. Since the dependence of the filter on the

Night	Date	$N_{H\alpha} \times 10^{-15}$ $ergcm^{-2}count^{-1}$	$N_{H\alpha r} \times 10^{-15}$ $ergcm^{-2}count^{-1}$	
1	10/7 - 11/7/1993	6.09±0.27	5.98±0.26	
2	11/7 - 12/7/1993	6.15±0.27	5.96±0.26	
3	12/7 - 13/7/1993	5.95±0.26	5.87±0.26	
4	13/7 - 14/7/1993	5.89±0.26	5.80±0.25	
5	18/7 - 19/7/1993	5.69±0.25	5.53±0.24	
6	19/7 - 20/7/1993	5.79±0.26	5.56±0.25	
7	20/7 - 21/7/1993	5.78±0.25	5.63±0.25	
8	21/7 - 22/7/1993	5.67±0.25	5.60±0.25	
9	23/7 - 24/7/1993	5.86±0.26	5.50±0.25	
10	24/7 - 25/7/1993	5.83±0.26	5.65±0.25	
		$N \times 10^{-15}$ $ergcm^{-2}count^{-1}$		
11	11/6 - 12/6/1994	6.89±0.59		
12	13/6 - 14/6/1994	6.37±0.37		
13	16/6 - 17/6/1994	6.08±0.27		
14	24/6 - 25/6/1994	6.37±1.00		
15	25/6 - 26/6/1994	6.14±0.69		
		$N_{H\alpha} \times 10^{-15}$ $ergcm^{-2}count^{-1}$	$N_{H\alpha r} \times 10^{-15}$ $ergcm^{-2}count^{-1}$	$N_{H\beta} \times 10^{-15}$ $ergcm^{-2}count^{-1}$
16	25/6 - 26/6/1995	3.38±0.15	3.30±0.15	4.77±0.21
17	01/7 - 02/7/1995	3.40±0.15	3.38±0.15	4.80±0.21
18	05/7 - 06/7/1995	3.39±0.15	3.34±0.15	-
19	06/7 - 07/7/1995	-	-	4.78±0.21
20	07/7 - 08/7/1995	3.38±0.15	3.37±0.15	-
21	09/7 - 10/7/1995	-	-	4.78±0.21

Table 5: Fluxes in $ergcm^{-2}count$ derived from dividing the theoretical fluxes by the observed fluxes of the standard stars for each observing night and each filter. These fluxes are used to calibrate the fluxes of the planetary nebulae from *counts* into $ergcm^{-2}sec^{-1}$.

calibration-flux, for the observing run of 1994, the errors in the calibration-fluxes are taken larger. These have been obtained with the B, V, R, Y and I filters. In the observing run of 1995 large differences between the calibration-fluxes $N_{H\alpha}$ and $N_{H\beta}$ are present.

2.9 Planetary nebulae photometry

The number of counts, exposure times and airmasses of the PNe are obtained with the same procedures as for the standard stars. The only difference is that for each

PN, instead of the 18 pixels for the standard stars, a different aperture, typically five times the FWHM of the PN, is chosen. For the $H\alpha$-, $H\beta$- and $OIII$-images of the PNe which are bright, large apertures that contain all the light are acceptable. Making an aperture list for these images shows that for increasing aperture an asymptotic number of counts is reached. For the $H\alpha r$-images of the PNe which are faint, small apertures, which will not contain all the light, are to be preferred (Howell, 1992).

Then, to obtain the nebular line fluxes of the PNe $F(H\beta)$, $F([OIII](5007))$ and $F(H\alpha)$ and the central star flux $F(H\alpha r)$ three corrections have to be made on the counts: (1) an exposure time correction, (2) an airmass correction and (3) a correction for the $[NII]6548$, $[NII]6584$ and HeI emission lines. So the actual flux $F(H\alpha)$ is equal to the calibrated flux,

$$\phi_{H\alpha} = \frac{C_{H\alpha}N_{H\alpha}}{t}(m \cdot e + 1)\frac{erg}{cm^2 s}, \tag{4}$$

minus the $[NII]$ emission,

$$F(H\alpha) = (\phi_{H\alpha} - [NII](6548) - [NII](6584))\frac{erg}{cm^2 s}, \tag{5}$$

where $C_{H\alpha}$ represents the counts of the PN in the $H\alpha$-filter, $N_{H\alpha}$ the calibration-flux, t the exposure time, m the airmass and e the atmospheric extinction. The actual flux $F(H\alpha r)$ is equal to the calibrated flux,

$$\phi_{H\alpha r} = \frac{CN_{H\alpha r}}{t}(m \cdot e + 1)\frac{erg}{cm^2 s}, \tag{6}$$

minus the HeI emission line,

$$F(H\alpha r) = (\phi_{H\alpha r} - HeI6678)\frac{erg}{cm^2 s}. \tag{7}$$

These equations can be rewritten to

$$F(H\alpha) = \frac{\phi_{H\alpha}}{1 + \frac{[NII](6548+6584)}{F(H\alpha)}}\frac{erg}{cm^2 s} \tag{8}$$

and

$$F(H\alpha r) = F(H\alpha)\left(\frac{\phi_{H\alpha r}}{F(H\alpha)} - \frac{HeI(6678)}{F(H\alpha)}\right) = F(H\alpha)\left(\frac{\phi_{H\alpha r}}{F(H\alpha)} - 0.0114\right)\frac{erg}{cm^2 s}, \tag{9}$$

taking a theoretical value of 0.0114 for the $HeI(6678)/F(H\alpha)$ line ratios. The $[NII](6548 + 6584)/F(H\alpha)$ line ratios are calculated under the assumption that $[NII](6584)/[NII](6548) = 3$. The ratios $[NII](6584)/H\alpha$ are taken from Acker

PNG	$\frac{[NII]}{F(H\alpha)}$	$C(H\alpha) \times 10^5$ $(counts)$	$C(H\alpha r) \times 10^4$ $(counts)$	$F(H\alpha) \times 10^{-13}$ $(ergcm^{-2}s^{-1})$	$F(H\alpha r) \times 10^{-14}$ $(ergcm^{-2}s^{-1})$	$t(s)$
000.0-06.8	1.011	21.10 ± 0.70	10.20 ± 0.50	54.21 ± 3.04	45.68 ± 3.44	1200
000.0-06.8	1.011	2.80 ± 0.50	2.55 ± 0.20	31.36 ± 7.46	48.28 ± 4.63	300
000.1-05.6	1.738	6.42 ± 0.30	0.58 ± 0.03	12.31 ± 0.81	1.60 ± 0.22	1200
000.1-05.6	1.738	1.25 ± 0.20	0.44 ± 0.02	3.29 ± 0.64	2.63 ± 0.20	900
000.7+04.7	1.148	1.83 ± 0.10	0.55 ± 0.03	4.25 ± 0.30	2.22 ± 0.20	1200
000.7+04.7	1.148	0.39 ± 0.02	0.55 ± 0.03	1.02 ± 0.17	2.59 ± 0.18	1200
001.2-03.0	0.921	1.06 ± 0.10		6.68 ± 0.66		600
001.4+05.3	0.255	4.84 ± 0.30	3.12 ± 0.20	19.66 ± 1.50	13.35 ± 1.24	1200
001.7-04.4	1.233	2.82 ± 0.20	1.26 ± 0.06	6.45 ± 0.55	5.43 ± 0.41	1200
001.7-04.4	1.233	1.89 ± 0.10	0.95 ± 0.02	6.40 ± 0.51	5.47 ± 0.28	900
003.4-04.8	0.049^r	8.39 ± 0.64	11.20 ± 0.75	54.33 ± 4.84	68.14 ± 6.06	900
003.4-04.8	0.049^r	1.21 ± 0.06	7.40 ± 0.50	14.04 ± 1.40	72.07 ± 5.82	600
004.2-05.9	0.460	13.40 ± 0.70	1.90 ± 0.10	47.55 ± 3.32	4.16 ± 0.77	1200
004.2-05.9	0.460	4.15 ± 0.50	1.43 ± 0.10	20.17 ± 2.60	7.32 ± 0.83	900
004.6+06.0	0.280	5.15 ± 0.30	2.68 ± 0.15	20.56 ± 1.52	10.95 ± 0.97	1200
004.6+06.0	0.280	0.71 ± 0.50	2.01 ± 0.10	4.01 ± 2.83	12.84 ± 0.91	900
005.1-03.0	0.417	6.20 ± 0.30	2.47 ± 0.10	23.10 ± 1.56	10.13 ± 0.82	1200
005.1-08.9	0.106	11.10 ± 0.50	1.80 ± 0.10	54.82 ± 3.51	3.23 ± 0.79	1200
005.1-08.9	0.106	3.14 ± 0.30	1.35 ± 0.10	20.91 ± 3.10	7.10 ± 0.87	900
005.1-08.9	0.106	2.54 ± 0.15	1.35 ± 0.10	18.47 ± 1.93	7.38 ± 0.82	900
008.4-03.6	0.869	8.83 ± 0.45	0.97 ± 0.05	24.77 ± 1.68	2.20 ± 0.39	1200
009.4-05.0	0.073	127.00 ± 7.00	45.70 ± 2.00	652.81 ± 46.92	171.74 ± 16.57	1200
009.4-05.0	0.073	5.32 ± 0.50	4.57 ± 0.50	301.20 ± 38.44	211.82 ± 29.01	120
009.4-05.0	0.073	10.40 ± 1.00	4.57 ± 0.50	543.75 ± 61.36	184.17 ± 29.52	120
009.4-05.0	0.073	11.70 ± 1.00	4.57 ± 0.50	584.42 ± 56.65	179.54 ± 29.40	120
009.4-05.0	0.073	6.61 ± 1.00	4.57 ± 0.50	354.95 ± 77.59	205.70 ± 30.01	120
009.4-05.0	0.073	9.87 ± 0.50	4.57 ± 0.50	496.84 ± 61.47	189.52 ± 29.53	120
065.0-27.3	0.011	3.85 ± 0.40	13.10 ± 3.00	15.47 ± 1.76	52.03 ± 12.59	900
108.4-76.1	0.156	2.05 ± 0.15	0.60 ± 0.10	10.55 ± 0.91	2.31 ± 0.62	600
125.9-47.0	-	4.02 ± 0.20	38.80 ± 2.00	18.34 ± 1.24	173.59 ± 12.18	800
351.2+05.2	1.427	32.50 ± 1.50	5.74 ± 0.30	69.12 ± 4.47	21.33 ± 2.06	1200
354.2+04.3	1.102	12.50 ± 0.50	4.45 ± 0.30	30.01 ± 1.82	18.33 ± 1.77	1200
354.9+03.5	1.022	2.13 ± 0.10	0.63 ± 0.03	5.35 ± 0.35	2.47 ± 0.21	1200
355.9-04.2	1.398	28.30 ± 2.00	7.54 ± 0.40	62.98 ± 5.29	32.49 ± 2.82	1200
356.5-03.9	0.736	12.30 ± 2.00	4.43 ± 0.20	28.01 ± 4.73	14.07 ± 1.25	900
356.8+03.3	1.487	1.75 ± 0.10	1.05 ± 0.05	3.57 ± 0.26	4.79 ± 0.34	1200
357.2+01.4	-	0.55 ± 0.03	0.29 ± 0.02	2.86 ± 0.20	1.10 ± 0.12	1200
358.0+02.6	-	1.39 ± 0.05	0.29 ± 0.02	6.94 ± 0.41	0.65 ± 0.13	1200
358.7+05.2	1.020	2.89 ± 0.20	1.39 ± 0.05	7.25 ± 0.60	5.94 ± 0.40	1200
358.8+04.0	0.333	1.42 ± 0.05	0.24 ± 0.02	5.40 ± 0.31	0.57 ± 0.12	1200
359.0+02.8	-	0.32 ± 0.01	0.30 ± 0.02	1.64 ± 0.09	1.26 ± 0.12	1200

Table 6: Fluxes of the planetary nebulae in $counts$ and in $ergcm^{-2}s^{-1}$ for the $H\alpha$ at $\lambda 6566 \AA$ and $H\alpha r$ at $\lambda 6648 \AA$ filters. The $[NII](6548{+}6584)/F(H\alpha)$-ratios are calculated from Acker et al. (1992) and Ratag (1991) (^{r}).

Name	$C(H\beta) \times 10^4$ *counts*	$t(s)$	$C([OIII]) \times 10^4$ *counts*	$t(s)$	$F(H\beta) \times 10^{-13}$ $ergcm^{-2}s^{-1}$	$F([OIII]) \times 10^{-13}$ $ergcm^{-2}s^{-1}$
001.2-03.0	11.40 ± 1.10	1800	0.98 ± 0.30	900	5.03 ± 0.65	0.86 ± 0.27
001.2-03.0	6.42 ± 0.60	1500	-	-	3.24 ± 0.36	-
001.7-04.4	1.43 ± 0.50	1800	-	-	0.64 ± 0.23	-
009.4-05.0	18.70 ± 1.00	300	-	-	49.30 ± 3.94	-
065.0-27.3	27.10 ± 3.00	1200	-	-	13.35 ± 1.60	-
108.4-76.1	5.64 ± 0.30	900	-	-	3.48 ± 0.24	-
356.5-03.9	8.13 ± 0.40	900	-	-	5.29 ± 0.36	-

Table 7: Fluxes of the planetary nebulae in counts and in $ergcm^{-2}s^{-1}$ obtained with the $H\beta$-filter, centered at a wavelength $\lambda 4856 \AA$ and the $OIII$-filter at $\lambda 5007 \AA$.

et al. (1992) and Ratag (1991). In the nebular line flux $F(H\beta)$ no other emission lines are present. But for the flux $F([OIII](5007))$ possibly some $F([OIII](4959))$ could be present depending on the shifting of the filter. However, the actual fluxes are taken to be

$$F(H\beta) = \frac{C_{H\beta} N_{H\beta}}{t}(m \cdot e + 1)\frac{erg}{cm^2 s}, \tag{10}$$

and

$$F([OIII](5007)) = \frac{C_{OIII} N}{t}(m \cdot e + 1)\frac{erg}{cm^2 s}. \tag{11}$$

The counts and actual fluxes obtained this way are listed in table 6 and 7. The errors in the counts are taken as five percent and larger if there are a lot of neighboring stars or saturation effects present. This latter effect is present in some of the $H\alpha$-counts, namely in the 1993 observations of PN G355.9-04.2, PN G000.0-06.8 and PN G003.4-04.8. For the latter two better doubles are present in the 1994 observations. PN G065.0-27.3 and PN G356.5-03.9 in the observing run of 1995 also showed small saturation effects. These effects are corrected for counting the number of bad pixels and adding peak values for these pixels to the counts. For the $H\alpha r$-counts in some cases nebular emission surrounds the star. A good example of this can be seen in the $H\alpha$- and $H\alpha r$-images of PN G005.1-08.9 (see figure 6). To correct for the nebular flux the $H\alpha r$-counts are measured with a smaller aperture. The errors in the actual fluxes are calculated accounting the errors in the counts, the calibration-fluxes and the atmospheric extinction. Note that for PN G001.2-03.0 no images taken with the $H\alpha r$-filter are available and that for PN G125.9-47.0, PN G357.2+01.4, PN 358.0+02.6 and PN G359.0+02.8 no $[NII](6548 + 6584)/F(H\alpha)$ line ratios could be obtained from the literature.

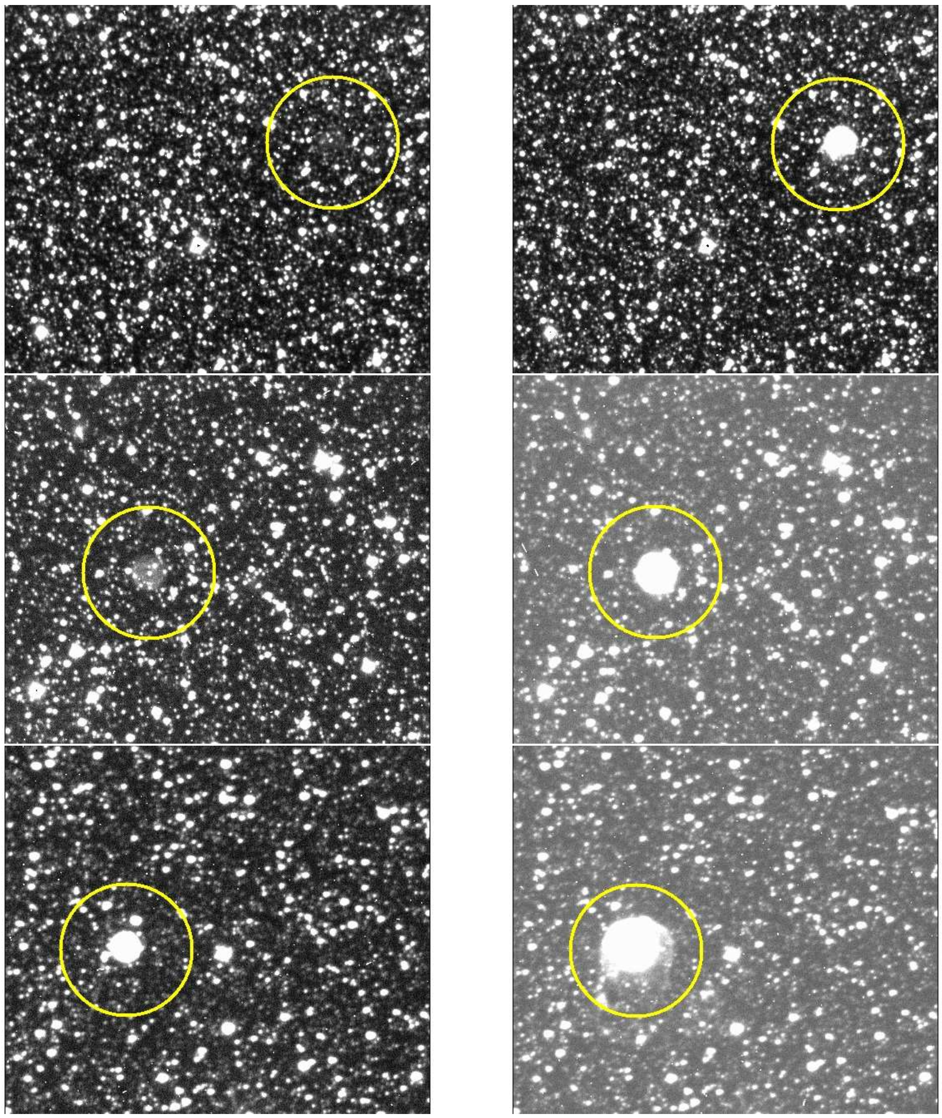

Figure 6: The processed CCD images with PN G000.1-05.6, PN G005.1-08.9 and PN G009.4-05.0 encircled (from top to bottom) in the narrow band $H\alpha r$-filter at $\lambda = 6647\mathring{A}$ (left) and the $H\alpha$-filter at $\lambda = 6566\mathring{A}$ (right). The difference between the star and nebular line flux is pronounced. For PN005.1-08.9 nebular line flux surrounds the star flux.

3 Theory

From the obtained fluxes the interstellar extinctions, stellar magnitudes, nebular line ratios, temperatures and luminosities can be determined. For the latter two the Zanstra method is used. From the diameters and expansion velocities of the nebulae ages can be obtained. This chapter shows how this is done.

3.1 Interstellar extinction

Four methods are used to obtain the interstellar extinction towards the planetary nebulae. A usual measure of the extinction towards a given star is the color excess $E(B-V)$, the excess of the blue minus visual magnitude of a star compared to the $B-V$ of a star with the same characteristics but without extinction. The flux at a certain wavelength is proportional to

$$F_\lambda \propto 10^{-\frac{A_\lambda E(B-V)}{2.5}}, \tag{12}$$

where A_λ is the extinction coefficient, which is a known function of wavelength. The values of this coefficient can be found in Pottasch (1984) and are fitted with a spline (see figure 7). From this plot the extinction coefficients at $H\beta$, $A_{4856} = 3.64$, at $[OIII]$, $A_{5007} = 3.49$, at the visual wavelength, $A_{5450} = 3.14$, at $H\alpha$, $A_{6566} = 2.51$ and at $H\alpha r$, $A_{6648} = 2.47$ are determined. To obtain the value of the color excess $E(B-V)$ for each individual nebula four methods are available: via the ratio of the $H\alpha$ flux and the $6cm$ or the $21cm$ radio flux, from the observed Balmer line ratios of $H\alpha/H\beta$ or from the dust map of Schlegel et al. (1998).

The first two methods for determining the extinction compare the radio continuum flux density with the $H\beta$ flux via

$$\frac{S_\nu}{F(H\beta)} = 2.51 \times 10^{10} T_e^{0.53} \nu^{-0.1} Y \frac{mJy}{ergcm^{-2}s^{-1}}, \tag{13}$$

where S_ν is the radio flux in mJy, Y the helium abundance and T_e the electron temperature of the nebula (Pottasch, 1984). Because both flux densities have the same dependence on density, the expected ratio is only a weak function of T_e and the helium abundance. Assuming that $T_e = 10,000$ K, $Y = 1.1$ and the theoretical line ratio $(H\alpha/H\beta)_{th} = 2.85$, for a nebula with this temperature and a density of $n_e = 10^4 cm^{-3}$, (Brocklehurst, 1971) it follows that

$$\frac{S_{6cm}}{F(H\alpha_{th})} = 1.09 \times 10^{12} \frac{mJy}{ergcm^{-2}s^{-1}}, \tag{14}$$

and

$$\frac{S_{21cm}}{F(H\alpha_{th})} = 1.23 \times 10^{12} \frac{mJy}{ergcm^{-2}s^{-1}}, \tag{15}$$

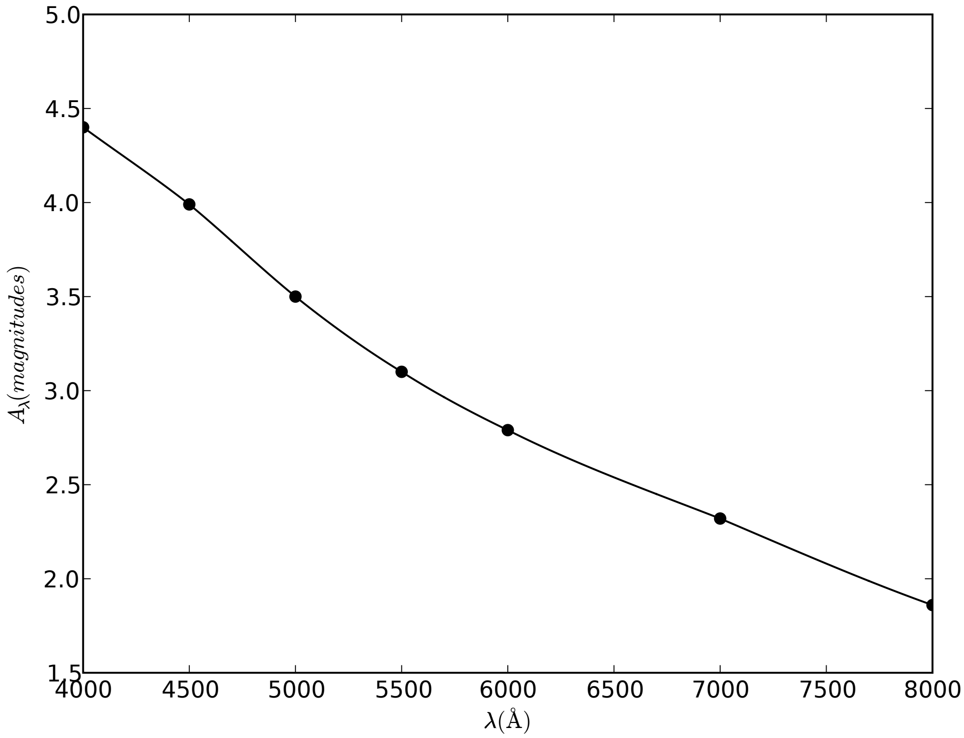

Figure 7: The extinction coefficient A_λ of interstellar dust as a function of wavelength. From this spline fitted through the data points (dots) obtained from Pottasch (1984) it is deduced that $A_{4856} = 3.64$, $A_{5007} = 3.49$, $A_{5450} = 3.14$, $A_{6566} = 2.51$ and $A_{6648} = 2.47$ magnitudes.

where the values of S_{6cm} can be found in Acker et al. (1992) and the values of S_{21cm} in Condon and Kaplan (1998). From equation 12, $A_{6566} = 2.51$ and $A_{H\alpha_{th}} = 0$ it follows that

$$\frac{H\alpha_{th}}{H\alpha_{obs}} = 10^{\frac{2.51E(B-V)}{2.5}} \tag{16}$$

and thus

$$E(B-V)(1) = \frac{2.5}{2.51}\log\left(\frac{S_{6cm}}{1.09 \times 10^{12} F(H\alpha)}\right), \tag{17}$$

and

$$E(B-V)(2) = \frac{2.5}{2.51}\log\left(\frac{S_{21cm}}{1.23 \times 10^{12} F(H\alpha)}\right). \tag{18}$$

These methods give the correct answer when the extinction occurs outside the nebula.

The observed relative intensities of the Balmer lines are expected to be independent of the electron density n_e and temperature T_e in the nebula. The third method to determine the extinction makes use of the observed Balmer line ratios $(H\alpha/H\beta)_{obs}$,

$$\left(\frac{H\alpha}{H\beta}\right)_{obs} = \left(\frac{H\alpha}{H\beta}\right)_{th}\left(\frac{H\beta_{th}}{H\beta_{obs}}\right)\left(\frac{H\alpha_{obs}}{H\alpha_{th}}\right) = 2.85 \cdot 10^{0.45E(B-V)}, \tag{19}$$

so that

$$E(B-V)(3) = \frac{1}{0.45}\log\left(\frac{1}{2.85}\cdot\left(\frac{H\alpha}{H\beta}\right)_{obs}\right). \tag{20}$$

These Balmer line ratios can be found in Acker et al. (1992).

The fourth method for determining the extinction makes use of the dust map Schlegel et al. (1998) produced. They processed far-infrared data of the Infrared Astronomy Satellite (IRAS) mission of 1983 and the DIRBE experiment (Diffuse Infrared Background Experiment) of 1989-1990 on board the COBE satellite into an uniform-quality column density map of the dust that radiates from 100 to $240\mu m$. These maps were obtained by removing zodiacal light contamination, as well as a possible cosmic infrared background (CIB). Testing these, assuming a standard reddening law, with the colors of elliptical galaxies to measure the reddening per flux density of $100\mu m$ emission, indicates that the maps are twice as accurate as the old Burstein-Heiles reddening estimates in regions of low and moderate reddening. The maps are expected to be significantly more accurate in regions of high reddening. Since there is a lot of dust present in the Galactic bulge, the $E(B-V)(4)$'s obtained from this map are likely to be accurate.

3.2 Stellar magnitudes

To determine the visual magnitudes of the central stars from the observed $H\alpha r$-flux the interstellar extinction difference between $H\alpha r$ at $6648\mathring{A}$ and the visual wavelength at $5450\mathring{A}$ and a Planck extrapolation factor need to be taken into account. The interstellar extinction difference can be written as

$$F_{vis} = F_{H\alpha r}10^{\frac{A_{6648}-A_{5450}E(B-V)}{2.5}} = F_{H\alpha r}10^{\frac{-0.662E(B-V)}{2.5}}. \tag{21}$$

The difference in the blackbody radiation at the two wavelengths is given by

$$\frac{B_{5450}}{B_{6648}} = \frac{\frac{2hc^2}{\lambda^5(e^{\frac{hc}{\lambda kT}}-1)}|_{\lambda=5450}}{\frac{2hc^2}{\lambda^5(e^{\frac{hc}{\lambda kT}}-1)}|_{\lambda=6648}} = \frac{\lambda^5(e^{\frac{hc}{\lambda kT}}-1)|_{\lambda=6648}}{\lambda^5(e^{\frac{hc}{\lambda kT}}-1)|_{\lambda=5450}}. \tag{22}$$

For a range of temperatures this ratio is plotted in figure 8. Since central star temperatures are roughly around $50,000$ K a ratio of $\frac{B_{5450}}{B_{6650}} = 2.1 \pm 0.1$ is adopted.

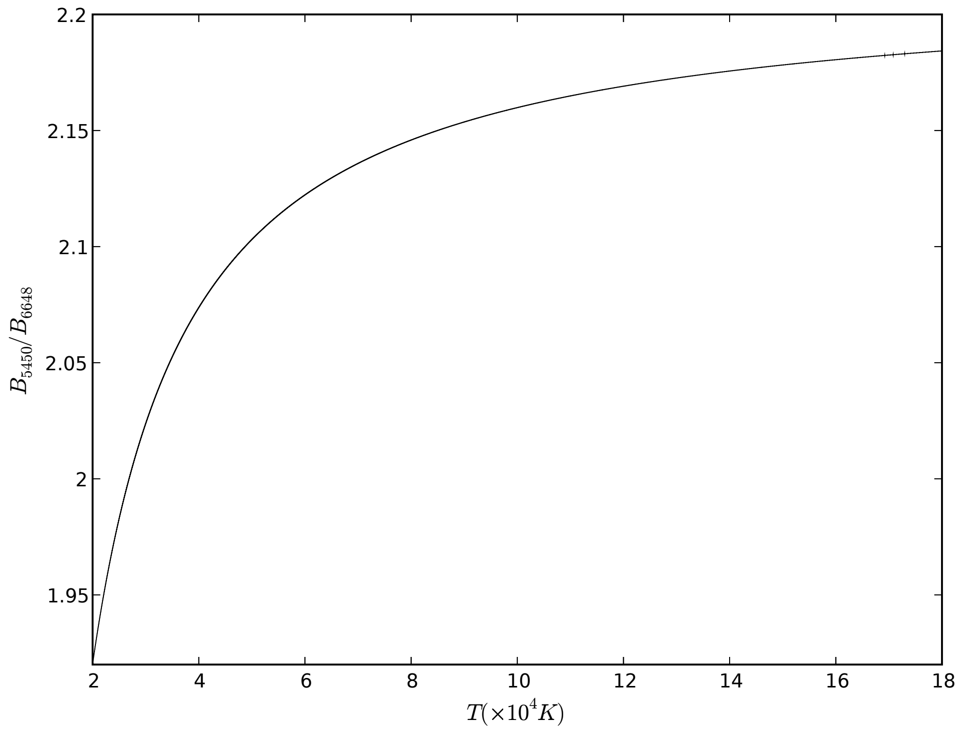

Figure 8: The ratio of the Planck function for the visual wavelength at $5450\mathring{A}$ and $H\alpha r$-wavelength at $6648\mathring{A}$ as a function of temperature.

Thus to obtain the visual fluxes, the fluxes measured at $H\alpha r$ need to be multiplied by the extinction differences found by radio S_{6cm} or S_{21cm} fluxes, the Balmer decrement or the Schlegel et al. (1998) map, $10^{-0.27E(B-V)(n)}$, and the ratio between the Planck functions, $\frac{B_{5450}}{B_{6650}} = 2.1 \pm 0.1$, and divided by the integrated width of the $H\alpha r$ filter, $FWHM_{H\alpha r} = 78.88\mathring{A}$. The visual fluxes obtained, which are in units of $ergcm^{-2}s^{-1}\mathring{A}^{-1}$, are transformed into magnitudes with

$$m_{vis} = -2.5 \log \left(\frac{F_{vis}}{3.64 \times 10^{-9}} \right). \tag{23}$$

Note that the magnitudes obtained this way are not corrected for the interstellar extinction but for the extinction difference between F_{vis} and $F_{H\alpha r}$.

3.3 Line ratios

Of some of the PNe in the sample also nebular line fluxes have been obtained in the narrow band filters $H\beta$ and $OIII$. For the calculation of the ratios of the nebular line fluxes, $H\alpha/H\beta$ and $[OIII](5007)/H\beta$, and the ratios of the stellar and nebular flux, $F_{vis}/H\beta$ and $F_{vis}/[OIII](5007)$, differences between the integrated widths of the filters need to be taken into account.

3.4 Zanstra temperatures

In 1931 Zanstra developed a ingenious method for determining the temperatures of the hot stars at the center of planetary nebulae. In his later years, he referred to this method as a 'cheap way to do space research'. It enables one to count the number of photons which can ionize hydrogen. These photons are shortward of $\lambda 912\mathring{A}$ and do not penetrate the atmosphere, hence the reference to 'space research'.

The assumption for this method to work is that the optical depth of the hydrogen ionizing radiation is greater than unity. This means that all the ionizing radiation of the star is absorbed by the nebula. For every ionizing photon, a

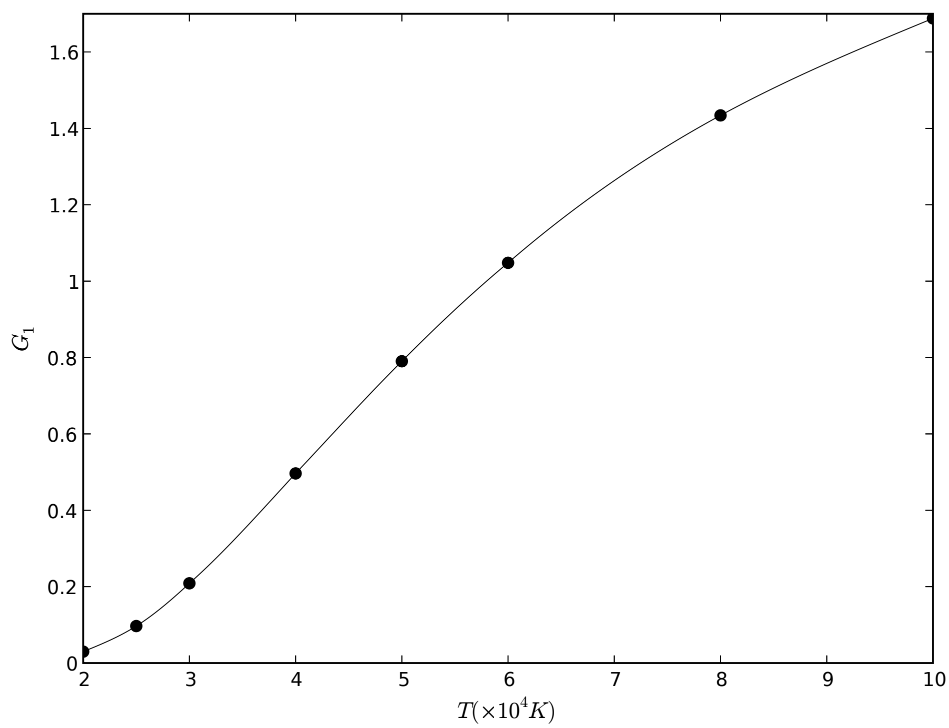

Figure 9: Spline fitted through numerical values from Pottasch (1984) of the integral G_1 used in determining the Zanstra temperature.

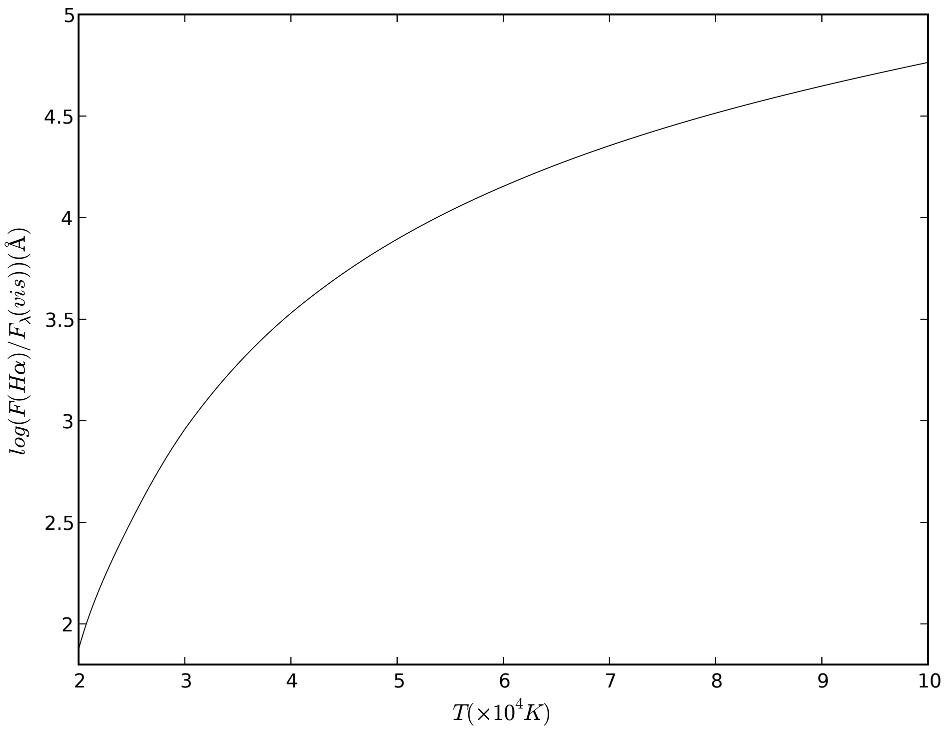

Figure 10: Theoretical ratios of $F(H\alpha)/F_\lambda(vis)$ as a function of temperature. By observing these ratios the Zanstra temperatures of the planetary nebulae are determined.

Balmer and a Lyα photon are produced. This way the number of ionizing photons coming from the central star can be estimated from the intensity of a Balmer line, $H\beta$ or $H\alpha$. The Zanstra temperature then can be derived by a comparison between the ionizing and the visual photons emitted by the star, assuming it radiates as a blackbody.

This theory can be quantized in the following equation

$$\frac{F(H\alpha)}{F_\lambda(vis)} = 1.13 \times 10^{-10} T^3 G_1(T) \left(e^{\frac{2.665 \times 10^4}{T}} - 1 \right) \mathring{A}, \tag{24}$$

where $F(H\alpha)$ is in units of $ergcm^{-2}s^{-1}$, while F_λ is in units of $ergcm^{-2}s^{-1}\mathring{A}^{-1}$, and G_1 is a known function of temperature (Pottasch, 1984). In figure 9 the values of G_1 are plotted and fitted with a spline. The values are put into equation 24, along with the temperatures. By making a plot with the ratio of $F(H\alpha)$ over $F_\lambda(vis)$ for every temperature in the range $2 \times 10^4 < T < 10 \times 10^4$ K, see figure 10, and determining this ratio for the objects the temperatures can be deduced.

3.5 Zanstra luminosities

To compute the luminosity of the central star the flux, the temperature and the distances have to be known. The distances of the PNe that are in the Galactic bulge are known with a error margin of 15 percent. Some of the distances are found in the catalogue of Acker et al. (1992). These are statistical distances and sometimes differ a lot. Then the value most closely to $8kpc$ is used. For the ones not listed in this catalogue a distance of $8kpc$ is chosen.

The central star flux arriving at the earth is

$$F_{vis} = \pi B_\lambda(T)\left(\frac{d}{R}\right)^2 ergcm^{-2}s^{-1}\mathring{A}^{-1}, \tag{25}$$

where $B_\lambda(T)$ is the Planck function at the visual wavelength at the temperature of the star in units of $ergcm^{-3}s^{-1}ster^{-1}$, d the distance to the nebula in units of cm, $1kpc = 3.086 \times 10^{21}cm$ and R the radius of the star in cm Rybicki and Lightman (1979).

Combining equation 28 with the Stefan-Boltzmann law, it follows that the luminosity,

$$\frac{L}{L_\odot} = \left(\frac{R}{R_\odot}\right)^2\left(\frac{T}{T_\odot}\right)^4 = \frac{F_{vis,int}}{\pi B_\lambda(T)}\left(\frac{d}{R_\odot}\right)^2\left(\frac{T}{T_\odot}\right)^4 \tag{26}$$

where $R_\odot = 6.96\times10^{10}cm$, $T_\odot = 5780$ K and $F_{vis,int}$ is the corrected for interstellar extinction, intrinsic visual flux, i.e. the observed visual flux times $10^{1.25E(B-V)}$.

3.6 Nebular ages

The nebular age is defined as the nebular radius divided by the present observed expansion velocity v_{exp}. The last parameter is usually not available for the bulge PNe. A catalogue, made by Weinberger (1988), of the expansion velocities of 288 Galactic PNe suggests that velocities are in the range of 7-30 km/s. Only for three objects in this sample, of which only PN G355.9-04.2 is in the bulge, the expansion velocity has been measured spectroscopically. In the literature commonly values of $20kms^{-1}$ are adopted. The uncertainty in the derived nebular ages introduced by this assumption is most likely within a factor two or three. Here a value of $15kms^{-1}$ will be adopted, following the work of Ratag (1991). By adopting a lower expansion velocity the theoretical ages of Blöcker (1995), which are generally overestimated, are allowed to have more chances to be reconciled with the observations.

4 Results

In this chapter the interstellar extinctions, stellar visual magnitudes, nebular line ratios, stellar to nebular line ratios, central star temperatures and luminosities and nebular ages are presented. The stellar magnitudes of the central stars are not corrected for interstellar extinction, the luminosities are. The results are compared with values found in the literature.

4.1 Interstellar extinctions

The interstellar extinctions calculated according to the radio flux densities, S_{6cm} and S_{21cm}, the Balmer line ratios and the dust map of Schlegel et al. (1998) are

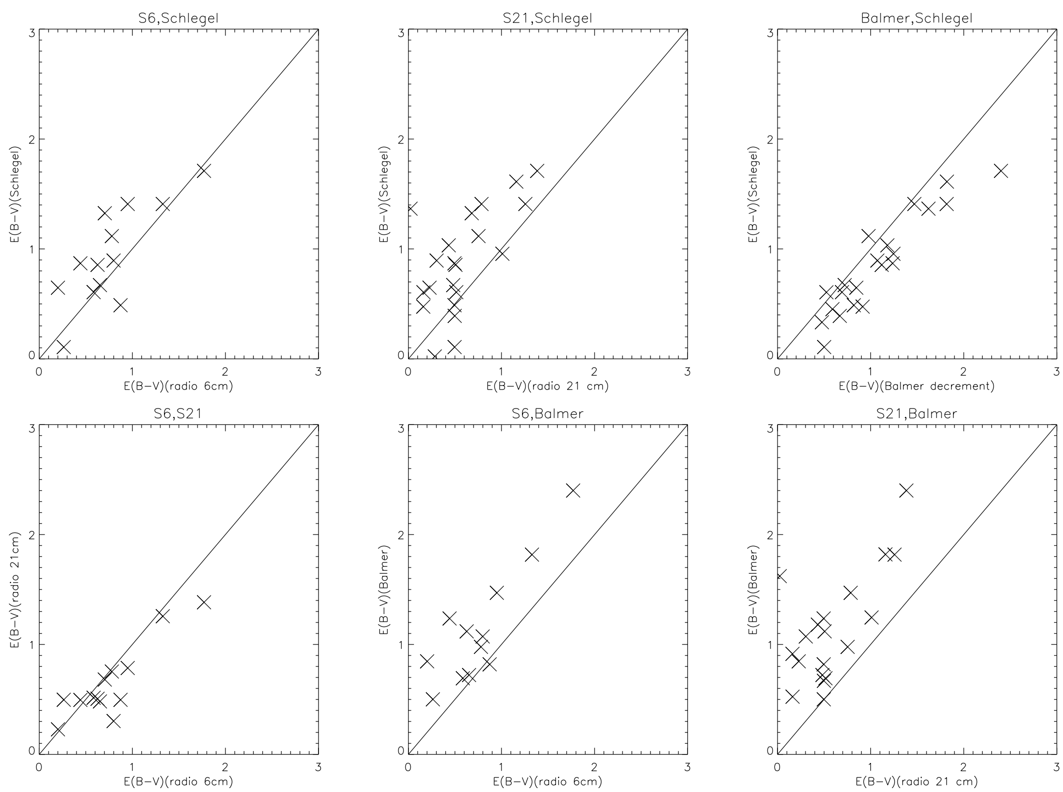

Figure 11: Comparison of the four methods used to determine the interstellar extinction $E(B-V)$. The extinctions determined with the dust map of Schlegel et al. (1998) and the Balmer line ratio method agree best with a one-to-one-correspondence. The extinctions determined with the radio $6cm$ and $21cm$ method, which also show good agreement, are significantly lower than the extinctions found by the Balmer line ratio method and the Schlegel dust map.

Name	$S_{6cm}(mJy)$	$S_{21cm}(mJy)$	$\frac{H\alpha}{H\beta}$	$E_{(B-V)}(1)$	$E_{(B-V)}(2)$	$E_{(B-V)}(3)$	$E_{(B-V)}(4)$
000.0-06.8	-	12.2 ± 0.6	5.70	-	0.50	0.67	0.39
000.1-05.6	-	2.2 ± 0.5	4.91	-	0.16	0.52	0.61
000.7+04.7	27.7	12.8 ± 0.9	34.27	1.77	1.38	2.40	1.71
001.2-03.0	-	8.5 ± 0.5	10.36	-	1.01	1.25	0.96
001.4+05.3	13.0	13.8 ± 0.6	7.85	0.78	0.75	0.98	1.12
001.7-04.4	5.3	2.5 ± 0.5	6.66	0.87	0.50	0.82	0.49
003.4-04.8	-	<2.5	7.35	-	0.16	0.91	0.47
004.2-05.9	-	<2.5	5.25	-	-0.37	0.59	0.45
004.6+06.0	14.2^s	5.1 ± 0.4	8.66	0.80	0.30	1.07	0.89
005.1-03.0	-	3.0 ± 0.5	15.30	-	0.02	1.62	1.37
005.1-08.9	-	4.4 ± 0.4	4.67	-	-0.18	0.48	0.33
008.4-03.6	-	8.3 ± 0.5	9.68	-	0.43	1.18	1.03
009.4-05.0	275.0	264.0 ± 9.4	5.84	0.58	0.51	0.69	0.61
009.4-05.0	275.0	264.0 ± 9.4	5.84	0.92	0.85	0.69	0.61
009.4-05.0	275.0	264.0 ± 9.4	5.84	0.66	0.59	0.69	0.61
009.4-05.0	275.0	264.0 ± 9.4	5.84	0.63	0.56	0.69	0.61
009.4-05.0	275.0	264.0 ± 9.4	5.84	0.85	0.78	0.69	0.61
009.4-05.0	275.0	264.0 ± 9.4	5.84	0.70	0.63	0.69	0.61
065.0-27.3	3.1	<6.0	4.79	0.26	0.50	0.50	0.11
108.4-76.1	-	<2.5	1.54	-	0.28	-0.59	0.02
351.2+05.2	12.0	14.4 ± 0.6	6.85	0.20	0.23	0.85	0.65
354.2+04.3	9.1	11.6 ± 0.6	10.26	0.44	0.50	1.24	0.87
354.9+03.5	-	9.6 ± 0.5	18.78	-	1.16	1.82	1.61
355.9-04.2	31.0	23.6 ± 0.8	6.02	0.65	0.48	0.72	0.67
356.5-03.9	13.0	11.1 ± 0.5	9.09	0.63	0.51	1.12	0.86
356.8+03.3	3.5	2.7 ± 0.5	13.07	0.95	0.79	1.47	1.41
358.7+05.2	17.0^s	16.3 ± 1.1	18.73	1.33	1.26	1.82	1.41
358.8+04.0	3.0	3.2 ± 0.5	-	0.70	0.68	-	1.33

Table 8: The radio $6cm$ and $21cm$ fluxes, from Acker et al. (1992) and Condon and Kaplan (1998) respectively and from Siodmiak et al. (2001) (^{s}), the $H\alpha/H\beta$-ratios, from Acker et al. (1992), the calculated extinctions and in the final column the extinctions $E(B-V)(4)$ from the dust map of Schlegel et al. (1998). The unphysical negative color excesses in the columns $E(B-V)(1)$, $E(B-V)(2)$ and $E(B-V)(3)$ are taken to be zero in further calculations.

listed in table 8. The unphysical negative extinctions in the columns $E(B-V)(1)$, $E(B-V)(2)$ and $E(B-V)(3)$ are taken to be zero in further calculations. The objects for which no $[NII](6548+6584)/F(H\alpha)$ line ratios could be obtained are removed from the sample. And if there were double values for $F(H\alpha)$ the ones with the longest exposure times are chosen. If saturation effects are present, the doubles with shorter exposure times are chosen. However the $H\alpha$-fluxes PN G 065.0-27.3, PN G 355.9-04.2 and PN G 356.5-03.9 are corrected for the saturation effects present, because no doubles are available. For PN G009.4-05.0 six values, obtained for different observation nights, are listed. Calculating the mean and error for these six gives $E(B-V)(1) = 0.72 \pm 0.12$ and $E(B-V)(2) = 0.65 \pm 0.12$. This indicates that the observations introduce a 15 to 18 percent uncertainty in the interstellar extinction.

In the literature hardly any interstellar extinctions are listed. For PN G009.4-05.0 extinctions $E(B-V)(1) = 0.56$ and $E(B-V)(3) = 0.65$ are found in Pottasch (1984), which corresponds well with the values listed here. For PN G065.0-27.3 extinctions $E(B-V)(1) = 0.11$ and $E(B-V)(3) = 0.08$ are found, which are much smaller than the values listed. Shaw and Kaler (1989) find that $E(B-V)(3) = 0.53$ and $E(B-V)(3) = 1.92$ for PN G009.4-05.0 and PN G358.7+05.2 respectively, which again corresponds well.

However, the extinctions determined with the dust map of Schlegel et al. (1998) and the radio $21cm$ method match remarkably well, see figure 11. The extinctions determined with the radio $6cm$ method and the Balmer line ratios, which also show good agreement, are significantly lower than the extinctions found by the radio $21cm$ method and the Schlegel dust map.

4.2 Nebular line fluxes

In table 9 the nebular line fluxes $F(H\beta)(4856)$ of six of the PNe are compared with those observed by Shaw and Kaler (1989). The $F(H\alpha)(6566)/F(H\beta)$-ratios are compared with the $H\alpha/H\beta$-ratios of Acker et al. (1992). For PN G001.2-03.0 the

PNG	$\log F(H\beta)(4856)$	$\log F(H\beta)$	$\frac{F(H\alpha)(6566)}{F(H\beta)}$	$\frac{H\alpha}{H\beta}$	$\frac{F([OIII])(5007)}{F(H\beta)}$
001.2-03.0	-12.49 ± 0.05	-12.61 ± 0.10	1.89 ± 0.19	10.36	0.35 ± 0.11
001.2-03.0	-12.36 ± 0.07	-12.61 ± 0.10	1.40 ± 0.14	10.36	0.26 ± 0.08
001.7-04.4	-13.19 ± 0.15	-12.61 ± 0.06	9.19 ± 0.78	6.66	-
009.4-05.0	-11.31 ± 0.03	-10.91 ± 0.06	12.11 ± 0.87	5.84	-
065.0-27.4	-11.87 ± 0.05	-12.10 ± 0.03	1.06 ± 0.12	4.79	-
108.4-76.1	-12.46 ± 0.03	-12.70 ± 0.10	2.78 ± 0.24	1.54	-
356.5-03.9	-12.28 ± 0.03	-12.58 ± 0.10	4.84 ± 0.82	9.09	-

Table 9: The logarithms of the nebular line fluxes $F(H\beta)(4856)$ compared to those observed by Shaw and Kaler (1989) and the $F(H\alpha)(6566)/F(H\beta)$-ratios compared with the $H\alpha/H\beta$-ratios of Acker et al. (1992) and the $F([OIII](5007))/F(H\beta)$-ratios. The ratios are corrected for the differences in the integrated widths of the filters. Note that the fluxes are uncorrected for interstellar extinction.

flux ratio $F([OIII])(5007)/F(H\beta)$ is listed as well. The ratios are corrected for the differences in the integrated widths of the filters, but the fluxes are uncorrected for interstellar extinction.

The nebular line fluxes $F(H\beta)$ agree within a factor of two with the fluxes found by Shaw and Kaler (1989). Comparing the $H\alpha/H\beta$-ratios with the values of Acker et al. (1992), it is indicated that the $H\alpha$-fluxes for PN G001.2-03.0 and PN G065.0-27.4 are a factor four too low, taking the factor two difference of the $H\beta$-fluxes into account. The $H\alpha$-fluxes of the other PNe are agreeable with the literature values, taking the factor two difference of the $H\beta$-fluxes into account. The flux $F([OIII])(5007)$ could possibly be contaminated with the emission of the $[OIII](4959)$-line.

4.3 Central star parameters

4.3.1 Stellar to nebula line ratios

In table 10 the ratios between the visual fluxes of the central star and the nebular lines are listed for six of the PNe. The visual fluxes have been obtained from the fluxes $F(H\alpha r)(6650)$ and are corrected for the extinction difference between $\lambda 6650\AA$ and the visual via the extinctions found in the Schlegel dust map. For PN G001.2-03.0 the visual flux is obtained from Acker et al. (1992). The ratios are corrected for the differences in the integrated widths. The $H\beta$-fluxes are compared with literature values in table 9. The visual magnitudes are compared in table 11. The visual fluxes found with the Schlegel extinctions of these six objects agree quite good with the literature, accept for PN G065.0-27.4 and PN G356.5-03.9, whose fluxes are a factor three and two brighter than found by Acker et al. (1992).

PNG	$\frac{F_{vis}(5450)}{F(H\beta)(4856)}$	$\frac{F_{vis}(5450))}{F([OIII])(5007))}$
001.2-03.0	0.18 ± 0.02	0.79 ± 0.27
001.2-03.0	0.28 ± 0.03	0.79 ± 0.27
001.7-04.4	1.25 ± 0.44	-
009.4-05.0	0.48 ± 0.04	-
065.0-27.4	0.73 ± 0.09	-
108.4-76.1	0.13 ± 0.01	-
356.5-03.9	0.32 ± 0.02	-

Table 10: The stellar fluxes relative to the nebular line fluxes for $F_{vis}(5450)/F(H\beta)(4856)$- and $F_{vis}(5450)/F([OIII])(5007)$-ratios, which are corrected for the differences in the integrated widths of the filters but uncorrected for interstellar extinction.

PNG	$m_{vis}(1)$	$m_{vis}(2)$	$m_{vis}(3)$	$m_{vis}(4)$	m_{vis}
000.0-06.8	-	13.96 ± 0.15	14.07 ± 0.15	13.89 ± 0.15	14.92
000.1-05.6	-	17.44 ± 0.19	17.68 ± 0.19	17.73 ± 0.19	-
000.7+04.7	18.15 ± 0.15	17.89 ± 0.15	18.56 ± 0.15	18.11 ± 0.15	-
001.2-03.0	-	-	-	-	16.20
001.4+05.3	15.54 ± 0.15	15.52 ± 0.15	15.67 ± 0.15	15.77 ± 0.15	16.30
001.7-04.4	16.58 ± 0.14	16.33 ± 0.14	16.54 ± 0.14	16.33 ± 0.14	16.57
003.4-04.8	-	13.30 ± 0.14	13.80 ± 0.14	13.51 ± 0.14	-
004.2-05.9	-	16.29 ± 0.23	16.68 ± 0.23	16.59 ± 0.23	16.80
004.6+06.0	15.77 ± 0.15	15.44 ± 0.15	15.95 ± 0.15	15.83 ± 0.15	-
005.1-03.0	-	15.34 ± 0.14	16.40 ± 0.14	16.23 ± 0.14	17.40
005.1-08.9	-	16.57 ± 0.29	16.88 ± 0.29	16.79 ± 0.29	-
008.4-03.6	-	17.27 ± 0.22	17.76 ± 0.22	17.67 ± 0.22	-
009.4-05.0	12.64 ± 0.15	12.59 ± 0.15	12.71 ± 0.15	12.65 ± 0.15	12.93, 12.82
009.4-05.0	12.63 ± 0.18	12.59 ± 0.18	12.48 ± 0.18	12.43 ± 0.18	12.93, 12.82
009.4-05.0	12.62 ± 0.21	12.57 ± 0.21	12.63 ± 0.21	12.58 ± 0.21	12.93, 12.82
009.4-05.0	12.62 ± 0.21	12.58 ± 0.21	12.66 ± 0.21	12.61 ± 0.21	12.93, 12.82
009.4-05.0	12.62 ± 0.19	12.57 ± 0.19	12.51 ± 0.19	12.46 ± 0.19	12.93, 12.82
009.4-05.0	12.61 ± 0.20	12.56 ± 0.20	12.60 ± 0.20	12.55 ± 0.20	12.93, 12.82
065.0-27.3	13.72 ± 0.28	13.88 ± 0.28	13.88 ± 0.28	13.62 ± 0.28	14.95
108.4-76.1	-	17.12 ± 0.31	16.93 ± 0.31	16.94 ± 0.31	-
351.2+05.2	14.65 ± 0.15	14.67 ± 0.15	15.08 ± 0.15	14.95 ± 0.15	16.20
354.2+04.3	14.97 ± 0.15	15.01 ± 0.15	15.50 ± 0.15	15.26 ± 0.15	-
354.9+03.5	-	17.63 ± 0.14	18.06 ± 0.14	17.93 ± 0.14	-
355.9-04.2	14.49 ± 0.14	14.38 ± 0.14	14.54 ± 0.14	14.50 ± 0.14	16.40
356.5-03.9	15.38 ± 0.15	15.30 ± 0.15	15.71 ± 0.15	15.54 ± 0.15	16.30
356.8+03.3	16.77 ± 0.13	16.66 ± 0.13	17.11 ± 0.13	17.07 ± 0.13	-
358.7+05.2	16.78 ± 0.13	16.74 ± 0.13	17.11 ± 0.13	16.84 ± 0.13	>17.20
358.8+04.0	18.91 ± 0.25	18.90 ± 0.25	-	19.33 ± 0.25	-

Table 11: The visual magnitudes of the central stars of the planetary nebulae, which are uncorrected for extinction, calculated from the $H\alpha r$ at $\lambda 6648 \AA$-fluxes with the four extinction differences between the visual and the reddened $H\alpha$, compared to literature values of respectively Acker et al. (1992) and Shaw and Kaler (1989).

4.3.2 Visual magnitudes

In table 11 the visual magnitudes are listed. They have been derived from the fluxes $F(H\alpha r)(6650)$, which are corrected for the extinction difference between $\lambda 6650 \AA$ and the visual via the extinctions found via the four methods. The errors are determined from the errors in the extinction, the Planck extrapolation factor and the flux. Compared to the literature values of Acker et al. (1992) and Shaw and Kaler (1989) most of the magnitudes found here are much brighter. The visual fluxes are for the most PNe a factor two or three and for PN G 355.9-04.2 even a factor five higher. Since the visual flux depends on the nebular line flux $F(H\alpha)$, if $F(H\alpha)$ increases $F(H\alpha r)$ increases, small saturation effects, which are corrected for, in the $H\alpha$-fluxes of PN G065.0-27.3, PN G355.9-04.2 and 356.5-03.9 could explain the discrepancy for some of the objects. However a comparison between the nebular line flux ratios $H\alpha/H\beta$ and the literature values indicates that PN G065.0-27.3 has a lower nebular line flux $F(H\alpha)$ instead of a higher one. A better explanation for the brighter values found lies in the fact that the literature values are obtained by directly measuring the V magnitude of the star with a Johnson V filter centered at $\lambda 5500\mathring{A}$ and a width of $890\mathring{A}$. The contribution of the visual continuum to the visual flux of the stars is large and is corrected for by calculating it and subtracting this from the visual flux. This method probably corrects for the continuum flux too great a value.

4.3.3 Zanstra temperatures

The Zanstra temperatures of the central stars are determined from the ratio of $F(H\alpha)/F_\lambda(vis)$, which are listed in table 12. The temperatures are shown in table 13 and logarithmically in table 14. The errors in the ratios are calculated according the errors in F_{vis} and $F(H\alpha)$. The temperatures are read from a table. The errors are estimated from this as well. The values are in agreement with the literature accept for PN G003.4-04.8, PN G065.0-27.3, PN G355.9-04.2 whose temperatures are $10,000$ K cooler. For PN G065.0-27.3 this is explained by the deduction from the nebular line ratios, that the flux $F(H\alpha)$ is a factor four lower than the literature value. The fact that the visual fluxes are brighter than the literature values also explain the lower temperatures.

4.3.4 Zanstra luminosities

The Zanstra luminosities calculated from the Zanstra temperatures and the statistical distances found in Acker et al. (1992) are listed in table 15. They have been corrected for the four interstellar extinctions. The errors are calculated from the errors in the temperature, visual flux and the distance. The values are in agreement with the literature. Note however that the variations in the extinctions determined with the four methods introduce more variation in the values of the luminosity.

4.3.5 Nebular ages

The nebular ages, $t1$ and $t2$ determined from the optical and radio diameters of the PNe respectively and the expansion velocities are shown in table 16. Only for three

PNe in this sample the expansion velocities are known. In the literature commonly values of $20 kms^{-1}$ are adopted for the expansion velocity. The uncertainty in the derived nebular ages introduced by this assumption is most likely within a factor two or three. Here a value of $15 kms^{-1}$ will be adopted, following the work of Ratag (1991). By adopting a lower expansion velocity the theoretical ages of Blöcker (1995), which are generally believed to be overestimated, are allowed to have more chances to be reconciled with the observations. If the radio and optical diameters differ, and thus the resulting ages, the highest age is adopted.

4.3.6 Positions of the stars in the Hertzsprung-Russell diagram

In figures 12, 13, 14 and 15 the $(\log T, \log L)$-values for the central stars of the PNe are plotted in a HR-diagram, indicating the errors and the nebular ages. The theoretical evolution tracks of Blöcker, from the five hydrogen burning models for core masses of 0.940, 0.836, 0.696, 0.625 and 0.605 $M_\odot$ and the helium burning model for the core mass 0.524 $M_\odot$, are shown in order to check if the theoretical ages agree with the nebular ages. According to the theory the high mass stars will have low ages and the low-mass stars will have high ages. Furthermore, this could be a check which of the four extinction methods is nearest to the truth. It is expected that none of the objects will be located above the 0.940 or down the 0.524 $M_\odot$ track. The luminous stars will spend too short a timescale on the horizontal track, that it is most unlikely they are included in this sample. Stars with extremely low luminosities would evolve so slowly that the surrounding nebula would have dispersed before the star reaches a temperature high enough to produce a significant amount of ionizing photons.

The positions of the stars determined with the radio $6cm$ method, which is only applicable to 12 of the objects, indeed fall inside this region, see figure 12. The nebular ages however are not consistent with the theoretical ages. The objects with their ages in purple, PN G009.4-05.0 and PN G355.9-04.2, indicate the nebular ages known with great certainty. At the 0.625 $M_\odot$ track PN G009.4-05.0 has an age of $4,000$ yr were an age of $1,000$ yr is expected. In the low-mass region PN G355.9-04.2 has a nebular age of 100 yr were a theoretical age of at least $9,000$ yr is expected. The objects in green with an uncertainty in age of a factor two to three are also significantly lower than the theory predicts. They are all low-mass stars with ages in the order of $500 - 2,000$ yr, accept for PN G358.8+04.0 having an age of $14,000$ yr, while theoretical ages of at least $7,000$ yr are expected. None of the objects are located in the high mass $0.696 - 0.940$ $M_\odot$ regions.

Four of the in total 23 objects, whose extinctions are determined with the radio $21cm$ method, are located in the *forbidden region* down below the 0.524 $M_\odot$ track, see figure 13. They are PN G000.1-05.6, PN G003.4-04.8, PN G005.1-08.9 and PN G008.4-03.6. For PN G003.4-04.8 the temperature compared to the literature value is $10,000$ K cooler. Making the temperature higher would increase the luminosity as well and the object is in the right region. The other three objects have high temperatures but low visual fluxes. Increasing the visual flux would decrease the temperature and the objects are even deeper in the forbidden region. It would mean that both the visual and $H\alpha$ flux have to increase to get these objects in the right region. The extinctions $E(B-V)(2)$ of these specific objects are much lower than the extinctions $E(B-V)(4)$, while the extinctions of the other objects agree closely. And the extinctions found with the Balmer method $E(B-V)(3)$ of these four objects do match the extinctions $E(B-V)(4)$. An increase of the extinction will also increase the luminosity. Thus, the fact that these four objects are in the forbidden region seems to be explained by their extinctions being too low. Again at the 0.625 $M_\odot$ track a nebular age of $4,000$ yr is located at a position where an age of $1,000$ yr is expected. And objects with nebular ages ranging from $500-2,000$ yr, accept for PN G358.8+04.0 having an age of $14,000$ yr, are located in the range of the low-luminosity-model where ages of at least $7,000$ yr are expected. None of the objects are located in the high mass $0.696-0.940$ $M_\odot$ regions.

Two of the in total 22 objects, whose extinctions are determined via the ratios of the Balmer line, are located in the *forbidden region* above the 0.904 $M_\odot$ track, see figure 13. These objects are PN G000.7+04.7 and PN G005.1-03.0. The visual flux and luminosity of PN G005.1-03.0 are higher than the literature values. But decreasing the visual flux, increases the temperature, which however does agree with the literature value. So for this object the visual and nebular line flux $F(H\alpha)$ need to decrease both. The extinctions $E(B-V)(3)$ of the objects are larger than the extinctions found with the other methods. Taking the extinctions $E(B-V)(4)$ instead would decrease the luminosity and the objects are in the right region. The objects have nebular ages of 500 and $1,000$ yr, where ages of 20 yr are expected. At the 0.696 $M_\odot$ track nebular ages of 200 and 400 yr are found, which agrees with the theoretical value of 200 yr, but also a nebular age of $4,000$ yr, which doesn't agree at all. At the 0.625 $M_\odot$ track three nebular ages of $1,000$ yr are found that agree with the theoretical value. A group of low-luminosity PNe have ages ranging from $500-2,000$ yr where ages of at least $7,000$ yr are expected.

None of the 23 objects, whose extinctions are determined via the dust map of Schlegel et al. (1998), are located in the forbidden region. This indicates that the resulting HR-diagram, see figure 15, is the most consistent one. Two objects at the 0.696 $M_\odot$ track have nebular ages of $1,000$ yr and $4,000$ yr, where theoretical ages of 200 yr are expected. The nebular age of only one object on the 0.625 $M_\odot$ track corresponds with the theory, having an age of $1,000$ yr. The lower mass objects have ages ranging from $500-2,000$ yr, accept for one object having an age of $14,000$ yr, where ages of at least $9,000$ yr are expected.

PNG	$\frac{F(H\alpha)}{F_\lambda(vis)}(1)$	$\frac{F(H\alpha)}{F_\lambda(vis)}(2)$	$\frac{F(H\alpha)}{F_\lambda(vis)}(3)$	$\frac{F(H\alpha)}{F_\lambda(vis)}(4)$
000.0-06.8	-	330 ± 91	366 ± 101	309 ± 85
000.1-05.6	-	3188 ± 588	3978 ± 734	4179 ± 771
000.7+04.7	2115 ± 320	1671 ± 253	3106 ± 470	2039 ± 308
001.2-03.0	586 ± 107	586 ± 107	586 ± 107	586 ± 107
001.4+05.3	890 ± 139	875 ± 137	1004 ± 157	1093 ± 171
001.7-04.4	760 ± 115	603 ± 91	735 ± 111	600 ± 91
003.4-04.8	-	80 ± 13	127 ± 20	98 ± 15
004.2-05.9	-	4289 ± 952	6144 ± 1363	5650 ± 1254
004.6+06.0	1147 ± 176	848 ± 130	1356 ± 208	1216 ± 186
005.1-03.0	-	868 ± 126	2301 ± 335	1969 ± 287
005.1-08.9	-	6375 ± 1730	8522 ± 2313	7808 ± 2119
008.4-03.6	-	5505 ± 1192	8679 ± 1879	7934 ± 1718
009.4-05.0	2039 ± 320	1954 ± 306	2177 ± 341	2067 ± 324
009.4-05.0	935 ± 198	896 ± 190	814 ± 173	773 ± 164
009.4-05.0	1662 ± 366	1592 ± 351	1691 ± 372	1605 ± 353
009.4-05.0	1798 ± 387	1723 ± 371	1864 ± 401	1770 ± 381
009.4-05.0	1087 ± 306	1041 ± 293	988 ± 278	938 ± 264
009.4-05.0	1511 ± 337	1448 ± 322	1501 ± 334	1425 ± 317
065.0-27.3	131 ± 37	151 ± 43	151 ± 43	119 ± 34
108.4-76.1	-	2038 ± 606	1714 ± 510	1737 ± 517
351.2+05.2	1376 ± 211	1398 ± 215	2039 ± 313	1805 ± 277
354.2+04.3	805 ± 122	832 ± 126	1307 ± 199	1044 ± 159
354.9+03.5	-	1651 ± 242	2470 ± 362	2176 ± 319
355.9-04.2	1083 ± 170	976 ± 153	1130 ± 177	1096 ± 172
356.5-03.9	1095 ± 236	1018 ± 219	1479 ± 319	1259 ± 271
356.8+03.3	499 ± 71	451 ± 64	685 ± 98	660 ± 94
358.7+05.2	1030 ± 151	986 ± 145	1388 ± 204	1082 ± 159
358.8+04.0	5455 ± 1290	5374 ± 1271	-	7962 ± 1884

Table 12: The observed $F(H\alpha)/F_\lambda(vis)$-ratios. The visual fluxes are calculated from the $H\alpha r$ at $\lambda 6648\mathring{A}$-fluxes and the four extinction differences between the visual and $H\alpha r$. These ratios are used to determine the temperature of the central stars.

PNG	$T_z(1) \times 10^3$ (kpc)	$T_z(2) \times 10^3$ (K)	$T_z(3) \times 10^3$ (K)	$T_z(4) \times 10^3$ (K)	$T_z \times 10^3$ (K)
000.0-06.8	-	25.0 ± 1.0	25.5 ± 1.0	25.0 ± 1.0	- - 30.2 -
000.1-05.6	-	39.5 ± 2.0	41.5 ± 2.0	42.0 ± 2.0	- - - -
000.7+04.7	36.0 ± 1.5	34.0 ± 1.5	39.0 ± 1.5	35.5 ± 1.5	- - - -
001.2-03.0	27.5 ± 1.0	27.5 ± 1.0	27.5 ± 1.0	27.5 ± 1.0	32.7 38.5 - -
001.4+05.3	30.0 ± 1.0	30.0 ± 1.0	30.5 ± 1.0	31.0 ± 1.0	- - - -
001.7-04.4	29.0 ± 1.0	28.0 ± 1.0	29.0 ± 1.0	28.0 ± 1.0	34.0 - - -
003.4-04.8	-	20.0 ± 0.5	21.5 ± 0.5	20.5 ± 0.5	- 31.9 - -
004.2-05.9	-	42.5 ± 2.0	46.5 ± 2.5	46.0 ± 2.5	- - - -
004.6+06.0	31.5 ± 1.0	29.5 ± 1.0	32.5 ± 1.0	32.0 ± 1.0	- - - -
005.1-03.0	-	30.0 ± 1.0	36.5 ± 1.0	35.5 ± 1.0	- 47.5 37.5 -
005.1-08.9	-	47.0 ± 4.0	51.0 ± 4.0	50.0 ± 4.0	- - - -
008.4-03.6	-	45.0 ± 3.5	51.5 ± 3.5	50.0 ± 3.5	- - - -
009.4-05.0	35.5 ± 1.5	35.5 ± 1.5	36.0 ± 1.5	35.5 ± 1.5	36.6 - - 35.0
009.4-05.0	30.0 ± 1.5	30.0 ± 1.5	29.5 ± 1.5	29.0 ± 1.5	36.6 - - 35.0
009.4-05.0	34.0 ± 2.0	34.0 ± 2.0	34.0 ± 2.0	34.0 ± 2.0	36.6 - - 35.0
009.4-05.0	34.5 ± 2.0	34.0 ± 2.0	35.0 ± 2.0	34.5 ± 2.0	36.6 - - 35.0
009.4-05.0	31.0 ± 2.5	31.0 ± 2.5	30.5 ± 2.5	30.0 ± 2.5	36.6 - - 35.0
009.4-05.0	33.5 ± 2.0	33.0 ± 2.0	33.0 ± 2.0	33.0 ± 2.0	36.6 - - 35.0
065.0-27.3	21.5 ± 0.5	22.0 ± 0.5	22.0 ± 0.5	21.5 ± 0.5	32.4 - - -
108.4-76.1	-	35.5 ± 2.5	34.0 ± 2.5	34.5 ± 2.5	- - -
351.2+05.2	32.5 ± 1.0	33.0 ± 1.0	35.5 ± 1.0	34.5 ± 1.0	37.6 39.0 36.5 -
354.2+04.3	29.5 ± 1.0	29.5 ± 1.0	32.5 ± 1.0	31.0 ± 1.0	- - - -
354.9+03.5	-	34.0 ± 2.0	37.0 ± 2.0	36.0 ± 2.0	- - - -
355.9-04.2	31.0 ± 1.0	30.5 ± 1.0	31.5 ± 1.0	31.0 ± 1.0	44.6 47.9 48.0 -
356.5-03.9	31.0 ± 1.5	31.0 ± 1.5	33.0 ± 1.5	32.0 ± 1.5	- - - -
356.8+03.3	27.0 ± 1.0	26.5 ± 1.0	28.5 ± 1.0	28.5 ± 1.0	- - - -
358.7+05.2	31.0 ± 1.0	30.5 ± 1.0	32.5 ± 1.0	31.0 ± 1.0	- - - $>$25.0
358.8+04.0	45.0 ± 3.0	45.0 ± 3.0	-	50.0 ± 3.0	- - -

Table 13: Zanstra temperatures of the central stars of the planetary nebulae obtained for the four extinctions compared to literature values of Mal'kov (1997), Ratag (1991), Pottasch and Acker (1989) and Shaw and Kaler (1989) respectively.

PN	$\log T_z(1)$ (K)	$\log T_z(2)$ (K)	$\log T_z(3)$ (K)	$\log T_z(4)$ (K)
000.0-06.8	-	4.40 ± 0.02	4.41 ± 0.02	4.40 ± 0.02
000.1-05.6	-	4.60 ± 0.02	4.62 ± 0.02	4.62 ± 0.02
000.7+04.7	4.56 ± 0.02	4.53 ± 0.02	4.59 ± 0.02	4.55 ± 0.02
001.2-03.0	4.44 ± 0.02	4.44 ± 0.02	4.44 ± 0.02	4.44 ± 0.02
001.4+05.3	4.48 ± 0.01	4.48 ± 0.01	4.48 ± 0.01	4.49 ± 0.01
001.7-04.4	4.46 ± 0.01	4.45 ± 0.02	4.46 ± 0.01	4.45 ± 0.02
003.4-04.8	-	4.30 ± 0.01	4.33 ± 0.01	4.31 ± 0.01
004.2-05.9	-	4.63 ± 0.03	4.67 ± 0.02	4.66 ± 0.02
004.6+06.0	4.50 ± 0.01	4.47 ± 0.01	4.51 ± 0.01	4.51 ± 0.01
005.1-03.0	-	4.48 ± 0.01	4.56 ± 0.01	4.55 ± 0.01
005.1-08.9	-	4.67 ± 0.04	4.71 ± 0.03	4.70 ± 0.03
008.4-03.6	-	4.65 ± 0.03	4.71 ± 0.03	4.70 ± 0.03
009.4-05.0	4.55 ± 0.02	4.55 ± 0.02	4.56 ± 0.02	4.55 ± 0.02
009.4-05.0	4.48 ± 0.02	4.48 ± 0.02	4.47 ± 0.02	4.46 ± 0.02
009.4-05.0	4.53 ± 0.03	4.53 ± 0.03	4.53 ± 0.02	4.53 ± 0.02
009.4-05.0	4.54 ± 0.03	4.53 ± 0.03	4.54 ± 0.02	4.54 ± 0.02
009.4-05.0	4.49 ± 0.04	4.49 ± 0.04	4.48 ± 0.03	4.48 ± 0.03
009.4-05.0	4.53 ± 0.03	4.52 ± 0.03	4.52 ± 0.03	4.52 ± 0.03
065.0-27.3	4.33 ± 0.01	4.34 ± 0.01	4.34 ± 0.01	4.33 ± 0.01
108.4-76.1	-	4.55 ± 0.03	4.53 ± 0.03	4.54 ± 0.03
351.2+05.2	4.51 ± 0.01	4.52 ± 0.01	4.55 ± 0.01	4.54 ± 0.01
354.2+04.3	4.47 ± 0.01	4.47 ± 0.01	4.51 ± 0.01	4.49 ± 0.01
354.9+03.5	-	4.53 ± 0.03	4.57 ± 0.02	4.56 ± 0.02
355.9-04.2	4.49 ± 0.01	4.48 ± 0.01	4.50 ± 0.01	4.49 ± 0.01
356.5-03.9	4.49 ± 0.02	4.49 ± 0.02	4.52 ± 0.02	4.51 ± 0.02
356.8+03.3	4.43 ± 0.02	4.42 ± 0.02	4.45 ± 0.01	4.45 ± 0.01
358.7+05.2	4.49 ± 0.01	4.48 ± 0.01	4.51 ± 0.01	4.49 ± 0.01
358.8+04.0	4.65 ± 0.03	4.65 ± 0.03	-	4.70 ± 0.03

Table 14: The logarithms of the Zanstra temperatures of the central stars of the planetary nebulae obtained for the four extinctions.

PNG	d (kpc)	$\log L_z(1)$ ($\frac{L}{L_\odot}$)	$\log L_z(2)$ ($\frac{L}{L_\odot}$)	$\log L_z(3)$ ($\frac{L}{L_\odot}$)	$\log L_z(4)$ ($\frac{L}{L_\odot}$)	$\log L_z$ ($\frac{L}{L_\odot}$)
000.0-06.8	8.0 ± 1.2	-	3.63 ± 0.15	3.81 ± 0.13	3.52 ± 0.13	-
000.1-05.6	6.4 ± 1.0	-	2.12 ± 0.16	2.53 ± 0.14	2.63 ± 0.14	-
000.7+04.7	8.0 ± 1.2	3.94 ± 0.15	3.49 ± 0.15	4.65 ± 0.13	3.86 ± 0.13	-
001.2-03.0	5.3 ± 0.8	3.02 ± 0.13	3.02 ± 0.13	3.02 ± 0.13	3.02 ± 0.13	3.72 2.79 - -
001.4+05.3	9.0 ± 1.3	3.64 ± 0.15	3.61 ± 0.15	3.85 ± 0.13	4.00 ± 0.13	-
001.7-04.4	7.1 ± 1.1	3.10 ± 0.15	2.69 ± 0.15	3.05 ± 0.13	2.68 ± 0.13	3.64 - - -
003.4-04.8	4.1 ± 0.6	-	2.67 ± 0.14	3.48 ± 0.12	3.00 ± 0.12	-
004.2-05.9	5.6 ± 0.8	-	2.59 ± 0.15	3.02 ± 0.14	2.87 ± 0.14	-
004.6+06.0	5.8 ± 0.9	3.25 ± 0.15	2.69 ± 0.15	3.55 ± 0.13	3.36 ± 0.13	- 3.19 - -
005.1-03.0	8.0 ± 1.2	-	2.67 ± 0.15	4.46 ± 0.13	4.18 ± 0.13	- 3.82 - -
005.1-08.9	4.5 ± 0.7	-	2.16 ± 0.20	2.73 ± 0.16	2.56 ± 0.16	-
008.4-03.6	4.0 ± 0.6	-	2.27 ± 0.18	3.17 ± 0.15	2.99 ± 0.15	-
009.4-05.0	3.8 ± 0.6	3.98 ± 0.15	3.92 ± 0.15	4.11 ± 0.13	4.01 ± 0.13	3.71 - - <3.55
009.4-05.0	3.8 ± 0.6	4.22 ± 0.16	4.15 ± 0.16	3.98 ± 0.14	3.88 ± 0.14	3.71 - - <3.55
009.4-05.0	3.8 ± 0.6	4.04 ± 0.17	3.98 ± 0.17	4.07 ± 0.14	3.99 ± 0.14	3.71 - - <3.55
009.4-05.0	3.8 ± 0.6	4.05 ± 0.17	3.96 ± 0.17	4.07 ± 0.14	3.97 ± 0.14	3.71 - - <3.55
009.4-05.0	3.8 ± 0.6	4.17 ± 0.15	4.10 ± 0.15	3.99 ± 0.13	3.91 ± 0.13	3.71 - - <3.55
009.4-05.0	3.8 ± 0.6	4.08 ± 0.17	3.99 ± 0.17	4.05 ± 0.14	3.97 ± 0.14	3.71 - - <3.55
065.0-27.3	8.4 ± 1.3	3.31 ± 0.17	3.57 ± 0.17	3.57 ± 0.15	3.16 ± 0.15	3.52 - - -
108.4-76.1	10.8 ± 1.6	-	2.73 ± 0.20	2.41 ± 0.16	2.44 ± 0.16	-
351.2+05.2	8.1 ± 1.2	3.27 ± 0.15	3.31 ± 0.15	4.00 ± 0.13	3.77 ± 0.13	3.49 3.15 3.10 -
354.2+04.3	7.6 ± 1.1	3.28 ± 0.15	3.33 ± 0.15	4.16 ± 0.13	3.75 ± 0.13	- 3.04 - -
354.9+03.5	8.0 ± 1.2	-	3.32 ± 0.16	4.06 ± 0.13	3.83 ± 0.13	-
355.9-04.2	3.0 ± 0.5	2.98 ± 0.15	2.80 ± 0.15	3.07 ± 0.13	3.00 ± 0.13	3.67 3.33 3.35 -
356.5-03.9	7.5 ± 1.1	3.39 ± 0.15	3.27 ± 0.15	3.95 ± 0.13	3.65 ± 0.13	-
356.8+03.3	8.0 ± 1.2	3.15 ± 0.15	2.97 ± 0.15	3.72 ± 0.13	3.66 ± 0.13	-
358.7+05.2	6.9 ± 1.0	3.63 ± 0.14	3.55 ± 0.14	4.17 ± 0.12	3.71 ± 0.13	-
358.8+04.0	8.0 ± 1.2	2.55 ± 0.18	2.53 ± 0.18	-	3.29 ± 0.15	-

Table 15: Distances, from Acker et al. (1992) or else taken as $8.0 \pm 1.2kpc$, and the logarithms of the Zanstra luminosities, corrected for the four extinctions, compared to the literature values of Mal'kov (1997), Ratag (1991), Pottasch and Acker (1989) and Shaw and Kaler (1989) respectively.

PNG	D_{opt} (arcsec)	D_{radio} (arcsec)	$D_{H\alpha}$ (arcsec)	v_{exp} (km/s)	$t1$ (kyr)	$t2$ (kyr)	$t3$ (kyr)	t (kyr)
000.0-06.8	0.0	0.0	12.4	15.0	0.002	0.000	2.492	-
000.1-05.6	12.4	0.0	16.4	15.0	1.997	0.000	2.634	2
000.7+04.7	2.7	1.5	6.6	15.0	0.544	0.302	1.335	.5
001.2-03.0	5.0	2.5	5.3	15.0	0.667	0.333	0.708	.5
001.4+05.3	5.0	4.3	8.8	15.0	1.128	0.970	1.994	1
001.7-04.4	5.0	2.5	5.7	15.0	0.893	0.447	1.027	1
003.4-04.8	9.0	3.4	7.1	15.0	0.936	0.353	0.735	1
004.2-05.9	6.0	0.0	10.2	15.0	0.838	0.000	1.420	1
004.6+06.0	8.6	4.7	7.5	15.0	1.264	0.691	1.104	1
005.1-03.0	6.3	0.0	5.7	15.0	1.269	0.000	1.157	1
005.1-08.9	18.6	0.0	22.1	15.0	2.107	0.000	2.503	2
008.4-03.6	7.6	0.0	15.0	15.0	0.771	0.000	1.524	1
009.4-05.0	15.5	0.0	31.8	6.0	3.667	0.000	7.529	4
065.0-27.3	1.0	3.0	4.4	15.0	0.211	0.633	0.932	.5
108.4-76.1	3.0	0.0	6.2	7.5	1.631	0.000	3.364	2
351.2+05.2	5.0	5.0	12.8	15.0	1.014	1.014	2.600	1
354.2+04.3	4.0	4.0	11.5	15.0	0.762	0.762	2.190	1
354.9+03.5	0.0	0.0	7.5	15.0	0.002	0.000	1.513	-
355.9-04.2	5.0	3.5	12.4	40.0	0.142	0.099	0.350	.1
356.5-03.9	5.0	1.7	7.1	15.0	0.948	0.322	1.340	1
356.8+03.3	0.0	1.2	6.2	15.0	0.002	0.242	1.246	.2
358.7+05.2	0.0	2.5	7.5	15.0	0.000	0.435	1.307	.4
358.8+04.0	70.0	60.0	8.4	15.0	14.095	12.081	1.691	14

Table 16: The ages $t1$, $t2$ and $t3$ calculated from the optical and radio diameters D_{opt} and D_{radio} from the literature and $D_{H\alpha}$ respectively and the expansion velocities v_{exp} and the ages t adopted in the Hertzsprung-Russell diagrams for determining the evolution of planetary nebulae.

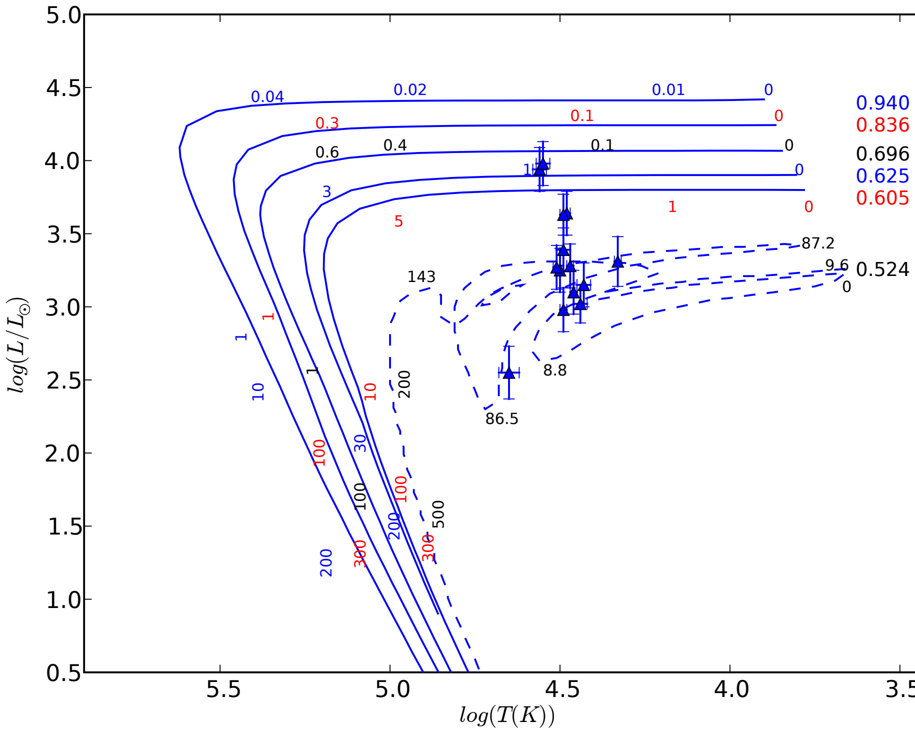

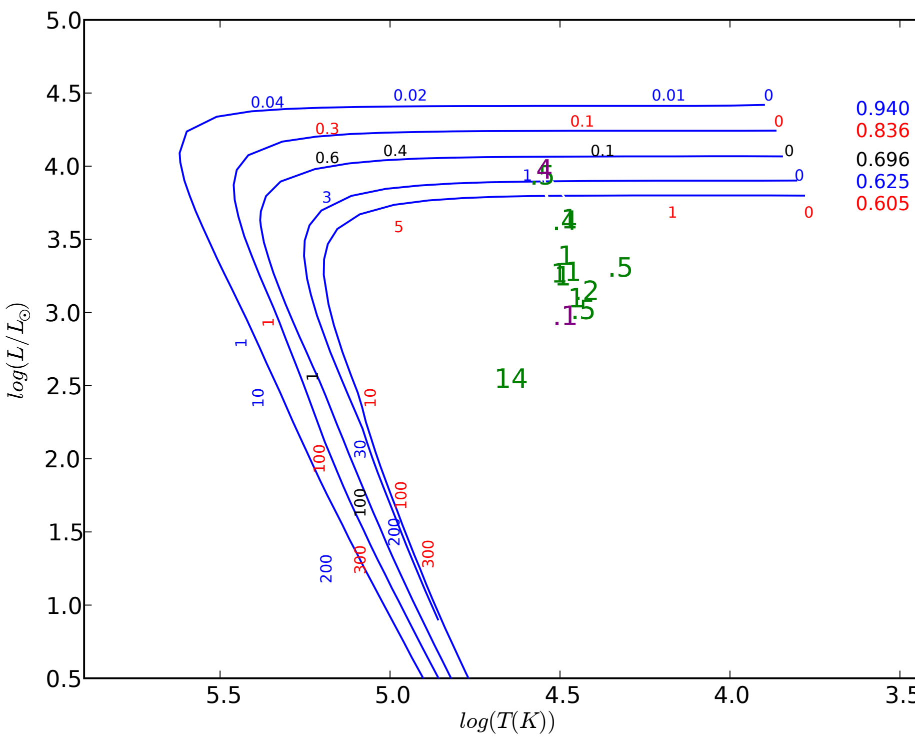

Figure 12: Hertzsprung-Russell diagram for the Zanstra luminosities determined with extinction E(B-V)(1) via the radio 6*cm* method, plotted indicating the error margins (top) and ages in 10^3 yr (bottom). The ages indicated in purple are known with greater certainty than the ones in green.

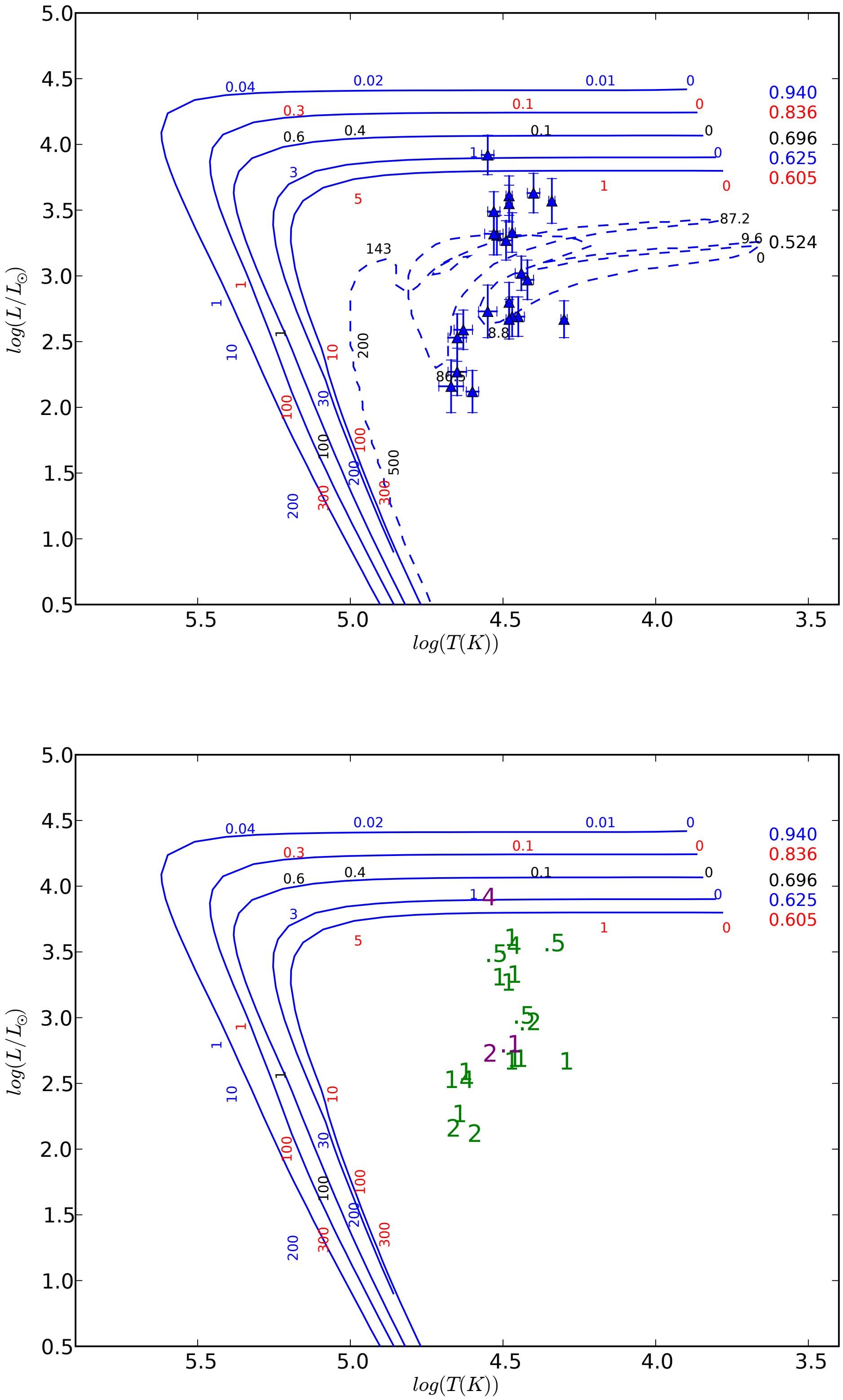

Figure 13: Hertzsprung-Russell diagram for the Zanstra luminosities determined with extinction E(B-V)(2) via the radio 21cm method, plotted indicating the error margins (top) and ages in 10^3 yr (bottom). The ages indicated in purple are known with greater certainty than the ones in green.

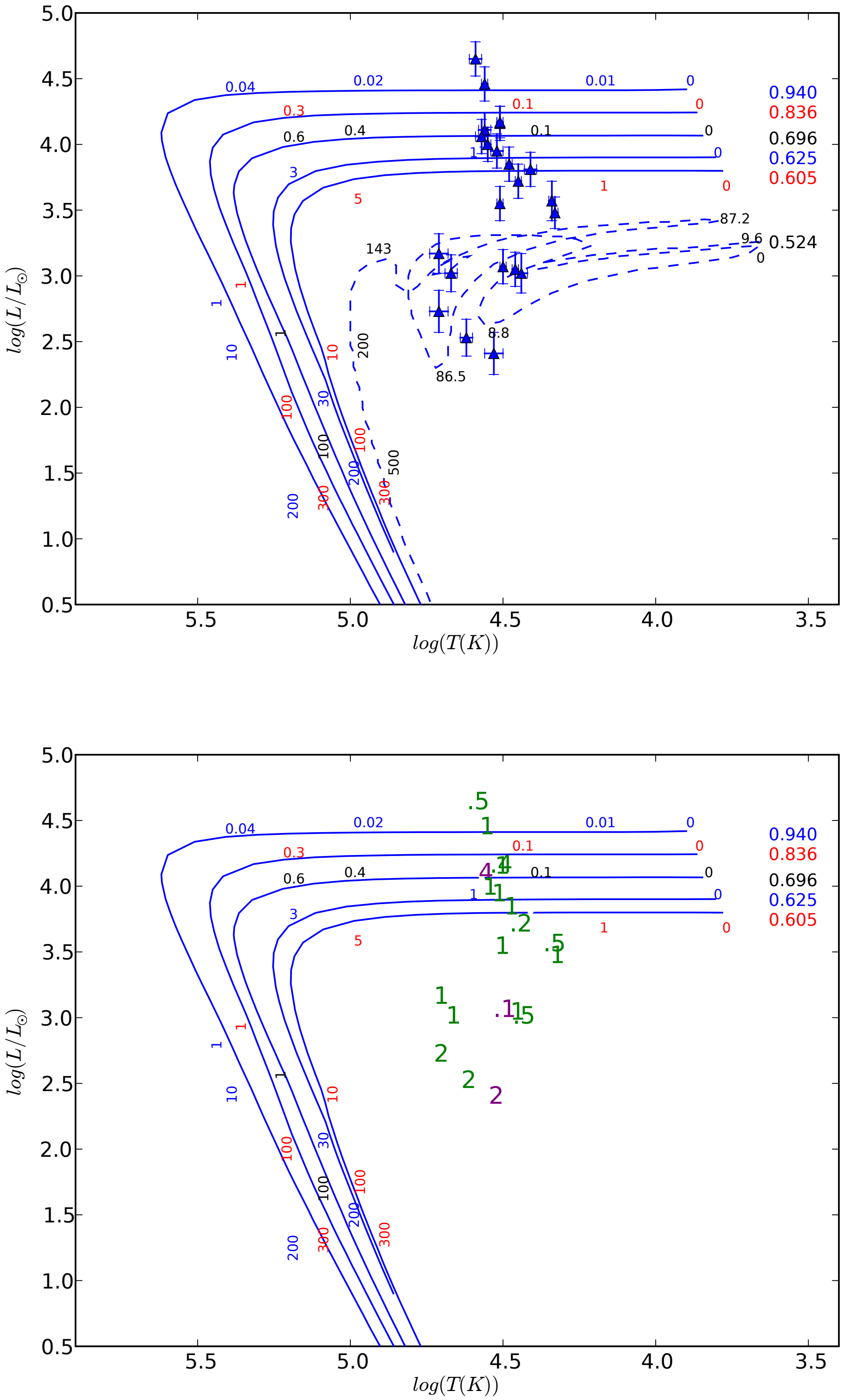

Figure 14: Hertzsprung-Russell diagram for the Zanstra luminosities determined with extinction E(B-V)(3) via the Balmer decrement method, plotted indicating the error margins (top) and ages in 10^3 yr(bottom). The ages indicated in purple are known with greater certainty than the ones in green.

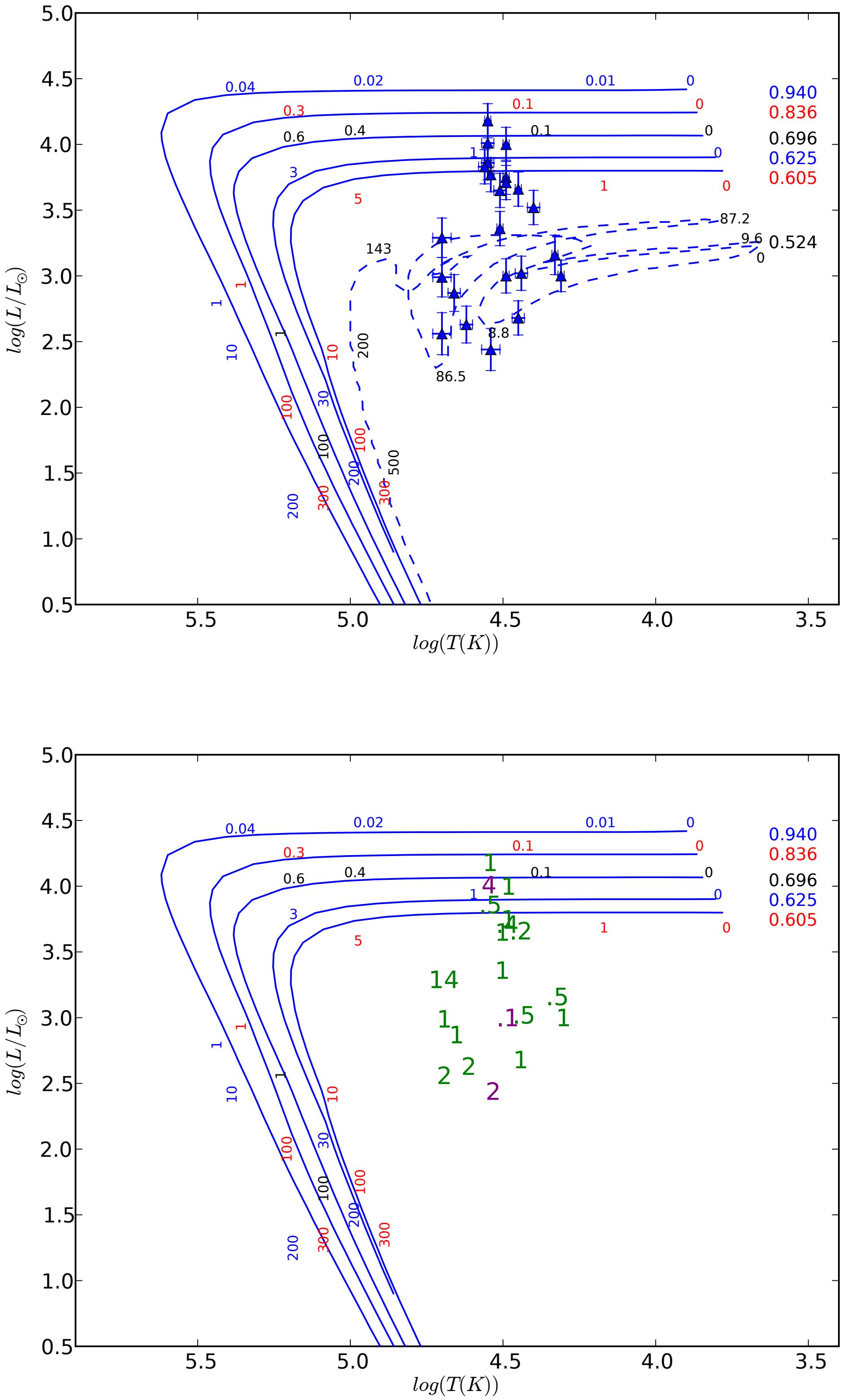

Figure 15: Hertzsprung-Russell diagram for the Zanstra luminosities determined with extinction E(B-V)(4) form the dust map of Schlegel et al. (1998), plotted indicating the error margins (top) and ages in 10^3 yr (bottom). The ages indicated in purple are known with greater certainty than the ones in green.

5 Discussion

Although the two most basic problems in determining the luminosity, namely distance and stellar flux uncertainties, are circumvented in this 'Groot onderzoek' a number of other uncertainties are still open. Is the assumption correct that the nebulae are optically deep for ionizing hydrogen photons? Do the stars radiate as a perfect blackbody? Which of the four used extinction measurements is the correct one?

The possibility still exists that a nebula is optically thick in most directions, but some radiation will escape accounted for in the Zanstra method. An extreme case might be that the actual temperature is $40,000$ K where as the Zanstra method yields $30,000$ K. In this case the luminosity would be a factor two too low.

The assumption that the central star emits like a blackbody is not certain at all. This could explain why the visual fluxes are brighter than those in the literature, which are obtained from a V filter and don't need to be transposed from one wavelength to the other. However, some values do agree with the literature.

That the positions of the stars are not certain at all follows also from the comparison of the four HR-diagrams for each of the methods, the extinctions determined with the Schlegel dust map seem to be the most consistent. They explain away the objects that are in the forbidden region for the Balmer and radio $21cm$ method. However for the Balmer method two nebular ages at the 0.696 and three at the 0.625 $M_\odot$ track agree with the theoretical ages. For the Schlegel dust map only one value at the 0.625 $M_\odot$ track agrees. For the radio $6cm$ and $21cm$ methods no matches are found and none of the objects lie in the high-mass $0.696 - 0.940$ $M_\odot$ region. From all the four HR-diagrams it can be concluded that the low-mass stars have nebular ages ranging from $500 - 2,000$ yr where ages of at least $7,000$ yr are expected. And under the assumption that the interstellar extinctions, obtained from the Balmer method and the dust map of Schlegel, result in the best HR-diagrams, it can be stated that at the 0.625 $M_\odot$ track theory is correct in predicting the ages. But for the high-mass $0.696 - 0.940$ $M_\odot$ region the nebular ages are larger than theory predicts.

It is certain this research shows that the theoretical evolution tracks of Blöcker predict too small ages for the low-mass objects. Since only two extinction methods predict it, it is a little riskier to say that for the 0.625 $M_\odot$ track nebular ages agree with that predicted from the theory or that objects in the high-mass $0.696 - 0.940$ $M_\odot$ region have larger observational ages than theory predicts. However the theory must be revised. The bulge is rich in binaries. Maybe the low ages of the low-mass objects are explained by the influence of companion stars, that invoke earlier envelope ejection. Or the mass loss laws are not correct. Or there are a lot more planetary nebula with helium burning central stars than expected.

6 Conclusions

Photometric reduction on a sample of 27 Galactic planetary nebulae has been performed successfully using IRAF. CCD images of the PNe have been made in narrow band filters $H\alpha$, $H\alpha r$, $H\beta$ and $OIII$ with the Dutch 91cm telescope in June/July 1993, 1994 and 1995. Furthermore images of Hamuy et al. (1992) and Landolt (1992) standard stars are obtained in the filters $H\alpha$, $H\alpha r$, $H\beta$, Y, U, B, V, R and I. These images are bias-subtracted and then flatfielded with a combined bias-subtracted flatfield for each specific filter for each of the 21 observing nights. Finally, the images are corrected for cosmic rays. Atmospheric extinction and filter information is obtained from ESO and effective airmasses are calculated with a macro. The photometric counts of the planetary nebulae are flux-calibrated using the calibration-fluxes deduced from the standard stars and corrected for the atmospheric extinction and the presence of emission lines.

From the obtained fluxes interstellar extinctions, visual magnitudes, nebular line and stellar to nebular line ratios, Zanstra temperatures and luminosities are deduced. The interstellar extinctions are determined with four methods. The extinctions determined with the dust map of Schlegel et al. (1998) and the radio $21cm$ method match remarkably well. The extinctions determined with the radio $6cm$ method and the Balmer line ratios, which also show good agreement, are significantly lower than the extinctions found by the radio $21cm$ method and the Schlegel dust map. Compared to the literature values some of the obtained visual fluxes are brighter a factor two, three and sometimes even a factor five. This is explained by the fact that the literature values are obtained by a direct measurement of the visual magnitude with a Johnson V filter. The contribution of the visual continuum to the visual flux of the stars is large and is corrected for by calculating and subtracting it from the total visual flux. Probably this method corrects for the continuum flux too great a value. The nebular line fluxes $F(H\beta)$ agree with the literature values within a factor two. The nebular line ratios $F(H\alpha)/F(H\beta)$ compared to the literature indicate that for some of the PNe the $H\alpha$-flux is a factor four too low taking into account the factor two difference in the $H\beta$-flux. The stellar to nebular line ratios $F_{vis}/F(H\beta)$ and $F_{vis}/F([OIII])$ are obtained for six of the PNe and are < 1. Three of the Zanstra temperatures of the central stars of 23 of the observed PNe have temperatures $10,000$ K cooler than the values found in the literature. This can either be explained by the nebular line flux $F(H\alpha)$ being too low or the visual fluxes being too bright. However, the Zanstra luminosities, which are corrected for interstellar extinction, match with the literature values available. However, the variations in the extinction determined with the four methods introduce more variation in the values of the luminosity.

Nebular ages have been obtained by dividing the optical and radio radii with the expansion velocity. Only for three PNe in this sample the expansion velocities are known. For the other objects values of $15km/s$ are adopted, which introduces a factor two to three uncertainty, while most commonly $20km/s$ is used. This in order to allow the theoretical ages of Blöcker (1995), which are generally overestimated, to have more chances to be reconciled with the observations.

Hertzsprung-Russell-diagrams of 23 central star temperatures and luminosities are compared with the theoretical evolution tracks of Blöcker (1995) for each of the four extinction methods. It is checked whether the nebular ages correspond with the theoretical ages predicted by the five hydrogen burning models for core masses of 0.940, 0.836, 0.696, 0.625 and 0.605 $M_{\odot}$ and the helium burning model for the core mass 0.524 $M_{\odot}$. It is expected that none of the objects will be located above the 0.940 or down the 0.524 $M_{\odot}$ track. For the extinctions determined with the radio $21cm$ none of the 12 objects falls inside the region. For the three other methods data is available for almost all of the objects. For the extinctions determined with the radio $6cm$ method four objects are positioned below the 0.524 $M_{\odot}$ track. The extinctions are a factor three smaller than the extinctions found via the Balmer line ratios and the dust map of Schlegel et al. For the extinctions determined with the Balmer line ratios, two of the objects are positioned above the 0.940 $M_{\odot}$ track. These objects have a factor one and a half higher extinctions than the extinctions found via the dust map of Schlegel et al (1998).

Comparing the four HR-diagrams for each of the methods, the extinctions determined with the Schlegel dust map seem to be the most consistent. They explain away the objects that are in the forbidden region for the Balmer and radio $21cm$ method. However for the Balmer method two nebular ages at the 0.696 and three at the 0.625 $M_{\odot}$ track agree with the theoretical ages. For the Schlegel dust map only one value at the 0.625 $M_{\odot}$ track agrees. For the radio $6cm$ and $21cm$ methods no matches are found and none of the objects lie in the high-mass $0.696 - 0.940$ $M_{\odot}$ region. From all the four HR-diagrams it can be concluded that the low-mass stars have nebular ages ranging from $500 - 2,000$ yr where ages of at least $7,000$ yr are expected. And under the assumption that the Balmer method and the dust map of Schlegel for determining the interstellar extinctions result in the best HR-diagrams, it can be stated that at the 0.625 $M_{\odot}$ track theory is correct in predicting the ages. And for the high-mass $0.696 - 0.940$ $M_{\odot}$ region the nebular ages are larger than theory predicts.

Although there are uncertainties in whether the PNe are optical deep for hydrogen ionizing photons and the positions in the HR-diagram are not all certain. It is certain to say that the theory on the evolution of planetary nebulae is correct for middle-mass objects but needs to be revised for low- and high-mass objects.

References

[1] Acker A. et al., *Strasbourg-ESO Catalogue of Galactic Planetary Nebulae*, ESO, 1992. Online at: http://vizier.u-strasbg.fr/viz-bin/VizieR

[2] Augusteijn, T. Melnick, J., Robledo E. and Schwarz, H.E. *The Dutch 91cm telescope*, ESO operating manual No. XX, version 1, October 1995.

[3] Bernard Salas, Jernimo *Physics and chemistry of gas in planetary nebulae*, PhD. Thesis,University of Groningen, 2003.

[4] Blöcker, T. *Stellar evolution of low- and intermediate-mass stars - Post-AGB evolution*, Astronomy and Astrophysics 299, 755-769, 1995.

[5] Brocklehurst, M. *Calculations of the level populations for the low levels of hydrogenic ions in gaseous nebulae*, Monthly Notices of the Royal Astronomical Society, 153, 471-490, 1971.

[6] Condon, J. J. and Kaplan, D. L. *Planetary Nebulae in the NRAO VLA Sky Survey*, Astrophysical Journal Supplement v.117, p.361, 07/1998.

[7] ESO, *ESO Filter System*, Online at: http://filters.ls.eso.org/

[8] ESO, *Optical and UV Spectrophotometric Standard Stars*, 2002 Online at: http://www.eso.org/observing/standards/spectra/

[9] Gathier, R., Pottasch, S.T., *Properties of planetary nebulae. II - Central star evolution*, Astronomy and Astrophysics (ISSN 0004-6361), vol. 209, no. 1-2, p. 369-381, January 1989.

[10] Hamuy, M. et al. *Southern spectrophotometric standards, 2*, Astronomical Society of the Pacific, Publications (ISSN 0004-6280), vol. 106, no. 700, p. 566-589, 1994.

[11] Howell, Steve B. *Astronomical CCD Observing and Reduction Techniques*, Astronomical Society of the Pacific conference series, ISSN 1050-3390 ; vol. 23, 1992.

[12] Landolt, A.U. *UBVRI photometric standard stars in the magnitude range* $11.5 < V < 16.0$ *around the celestial equator*, Astron. J., 104, 340-371,1992.

[13] Mal'kov Y.F., *A self-consistent determination of the distances, physical parameters, and chemical composition for a large sample of Galactic planetary nebulae: the distances and parameters of central stars and the optical depths of envelopes*, Astron. Rep., 41, 760-776, 1997.

[14] Massey, Philip *A User's Guide to CCD Reductions with IRAF*, Online at: http://iraf.noao.edu/iraf/ftp/iraf/docs/ccduser2.ps.Z, February 15, 1997.

[15] Massey, Philip and Davis, Lindsey E. *A User's Guide to Stellar CCD Photometry with IRAF*, Online at: http://iraf.noao.edu/iraf/ftp/iraf/docs/daophot2.ps.Z, April 15, 1992.

[16] Mendez, R.H., Kudtitzki, R.P., Herrero, A., Husfeld, D., Groth, H.G.,*High resolution spectroscopy of central stars of planetary nebulae. I - Basic atmospheric parameters and their interpretation*, Astronomy and Astrophysics, vol. 190, no. 1-2, p. 113-136, January 1988.

[17] Pottasch, S.R. *Planetary Nebulae, A Study of Late Stages of Stellar Evolution*, D.Reidel Publishing Company, Dordrecht, Holland, 1984.

[18] Pottasch, S.R. and Acker, A. *Evolution of planetary nebulae in the galactic bulge*, Astronomy and Astrophysics 221, 123-129, 1989.

[19] Ratag, M.A. *A study of Galactic Bulge Planetary Nebulae*, PhD. Thesis, University of Groningen, 1991.

[20] Rybicki, George B. and Lightman, Alan P. *Radiative processes in astrophysics*, John Wiley and Sons, Inc., United States of America, 1979.

[21] Schlegel, David J., Finkbeiner, Douglas P. and Davis, Marc *Maps of dust infrared emission for use in estimation of reddening and cosmic microwave background radiation foregrounds*, The Astrophysical Jornal, 500:525-553, 1998 June 20.

[22] Shaw, Richard A. and Kaler, James B. *Apparent magnitudes of luminous planetary nebulae nuclei - II A survey of southern hemisphere planetary nebulae*, The Astrophysical Journal Supplement Series, 69:495-424, 03/1989.

[23] Siodmiak N., Tylenda R. *An analysis of the observed radio emission from planetary nebulae*, Astronomy and Astrophysics 373, 1032, 2001.

[24] Tug, H. *Vertical extinction on La Silla*, ESO Messenger, vol. 11, p. 7-8, 1977.
Online at: http://www.ls.eso.org/lasilla/Telescopes/2p2T/D1p5M/misc/Extinction.html

[25] Vreeswijk, Paul *Central Star Parameters of a sample of Galactic Bulge Planetary Nebulae - Klein Onderzoek report*, Groningen, January 17, 1995.

[26] Weidemann, V. *The initial-final mass relation: Galactic disk and Magellanic Clouds*, Astronomy and Astrophysics, 188, 74-84, 1987.

[27] Weinberger, R. *A catalogue of expansion velocities of Galactic planetary nebulae*, Astronomy and Astrophysics Supplement Series, vol. 78, no. 2, p. 301-324, May 1989.

Appendix

A Error analysis

Instrumental uncertainties, fluctuations in measurements due to finite precision of measuring instruments, are calculated with the formula,

$$s^2 = \frac{1}{N-1}\sum(x_i - \bar{x})^2, \tag{27}$$

where N is the number of data points, x_i the value of the data point and $\bar{x}$ is the mean value, calculated with

$$\overline{x} = \frac{\sum x_i}{N} \tag{28}$$

The propagation of errors is calculated, assuming x is a function of u and v, $x = f(u, v)$, with

$$\sigma_x^2 = \sigma_u^2\left(\frac{\partial x}{\partial u}\right)^2 + \sigma_v^2\left(\frac{\partial x}{\partial v}\right)^2 + 2\sigma_{uv}^2\left(\frac{\partial x}{\partial u}\right)\left(\frac{\partial x}{\partial v}\right) \tag{29}$$

If u and v are uncorrelated, then $\sigma_{uv} = 0$.